Contributions to Mineralogy and Petrology (2024) 179:62
https://doi.org/10.1007/s00410-024-02143-y

ORIGINAL PAPER

Laser ablation (in situ) Lu-Hf geochronology of epidote group minerals

Jie Yu[1,2,3] · Stijn Glorie[1,2] · Martin Hand[1,2] · Alexander Simpson[1] · Sarah Gilbert[4] · Kristoffer Szilas[5] · Nick Roberts[6] · Mark Pawley[7] · Yanbo Cheng[8]

Received: 3 January 2024 / Accepted: 17 May 2024

Abstract

Epidote group minerals, including allanite, clinozoisite and epidote are common in a range of metamorphic, igneous and hydrothermal systems, and are stable across a wide range of pressure–temperature (*P–T*) conditions. These minerals can incorporate substantial amounts of rare earth elements (REEs) during their crystallisation, making them potential candidates for Lu–Hf geochronology to provide age constraints on various geological processes. Here we report on a first exploration into the feasibility of in situ Lu–Hf geochronology for epidote group minerals from various geological settings and compare the results with age constraints from other geochronometers. Magmatic allanite samples from pegmatites and monzogranites in the Greenland anorthosite complex, Coompana Province and Qingling Orogen provided dates consistent with magmatic events spanning from c. 2660 to 1171 Ma. In the Qingling pegmatites, a younger phase of hydrothermal allanite was dated at c. 215 Ma, consistent with the timing of regional REE mineralisation. Allanite from the Yambah Shear Zone, Strangways Metamorphic Complex, yielded Lu–Hf age of c. 430 Ma. It predates the garnet and apatite growth at c. 380 Ma, suggesting the Lu–Hf system can be preserved in allanite during prograde amphibolite-facies metamorphism. Additionally, Lu–Hf dates for hydrothermal clinozoisite and epidote are consistent with the timing of hydrothermal alteration and mineralisation in a range of settings, demonstrating the utility of the technique for mineral exploration. Despite the current lack of matrix-matched reference materials, the successful application of laser ablation Lu–Hf geochronology to epidote group minerals offers valuable geochronological insights into various geological processes that can be difficult to access through other geochronometers.

Keywords Lutetium-hafnium · in situ geochronology · Epidote · Allanite · Clinozoisite · Rare earth elements

Communicated by Othmar Müntener.

✉ Jie Yu
jie.yu1@curtin.edu.au

[1] Department of Earth Sciences, The University of Adelaide, Adelaide, SA 5005, Australia

[2] Mineral Exploration Cooperative Research Centre, Kensington, WA 6151, Australia

[3] School of Earth and Planetary Sciences, Curtin University, Perth, WA 6845, Australia

[4] Adelaide Microscopy, The University of Adelaide, Adelaide, SA 5005, Australia

[5] Department of Geosciences and Natural Resource Management, University of Copenhagen, Øster Voldgade 10, Copenhagen 1350, Denmark

[6] Geochronology and Tracers Facility, British Geological Survey, Keyworth, Nottingham NG12 5GG, UK

[7] Department for Energy and Mining, Geological Survey of South Australia (GSSA), 11 Waymouth Street, Adelaide, SA 5001, Australia

[8] Geoscience Australia, GPO Box 378, Canberra, ACT 2601, Australia

Published online: 25 May 2024

Introduction

Epidote group minerals e.g., epidote, clinozoisite and allanite, exhibit stability across an extensive range of *P–T* conditions (Franz and Liebscher 2004; Grapes and Hoskin 2004). Their structural formula is represented as $A_2M_3(SiO_4)(Si_2O_7)(O, F)(OH)$, or in a simplified form, $A_2M_3Si_3O_{11}(O, F)(OH)$, where A = Ca, Sr, Pb^{2+}, Mn^{2+}, Th, REE^{3+}, and U, and M = Al, Fe^{3+}, Fe^{2+}, Mn^{3+}, Mn^{2+}, Mg, Cr^{3+}, and V^{3+} (Deer et al. 1986). Epidote and clinozoisite are the most prevalent members of the epidote group minerals and often form continuous solid solution series of $Ca_2Al_3Si_3O_{11}(O, F)(OH)$–$Ca_2Fe_3Si_3O_{11}(O, F)(OH)$, facilitated by the substitution of Fe for Al (Franz and Liebscher 2004). Allanite is the REE-rich member of the epidote group, with trivalent REE occupying the A sites and charge-balanced by a divalent cation (Fe^{2+}, Mn^{2+}, Mg) substituting for a trivalent one in the M sites, forming the idealized formula of $CaREEAl_2FeSi_3O_{11}O(OH)$ (Gieré and Sorensen 2004). Epidote group minerals are commonly associated with metamorphic rocks, and also frequently occur in igneous rocks and hydrothermal mineral deposits (Bird and Spieler 2004; Enami et al. 2004; Grapes and Hoskin 2004; Schmidt and Poli 2004), and thus hold great geological and economic importance. For instance, epidote is a representative mineral in the propylitic alteration zone associated with porphyry systems and the calcic alteration zone in iron-oxide copper gold (IOCG) systems (Groves et al. 2010; Sillitoe 2010). Its distribution and trace element composition can serve as valuable indicators for mineral exploration (e.g., Cooke et al. 2014; Pacey et al. 2020; Schlegel et al. 2022). Epidote, clinozoisite and allanite can remain stable during zeolite- to amphibolite-facies metamorphism in contact and regional metamorphic terranes (Franz and Liebscher 2004; Gieré and Sorensen 2004; Grapes and Hoskin 2004), providing crucial constraints on the *P–T* conditions and geological evolution history (Janots et al. 2008, 2009; Gabudianu Radulescu et al. 2009; Spear 2010; Janots and Rubatto 2014; Boston et al. 2017). Furthermore, allanite can occur in abundance in certain carbonatites and pegmatites, forming economic mineralisation that can be mined for critical REEs and uranium (e.g., Li and Zhou 2018; Wei et al. 2023).

In recent years, there have been significant advancements in epidote group minerals geochronology. Among these minerals, allanite stands out as it contains the highest concentrations of Th and U within the epidote group minerals (typically 0.05–3 wt% Th and 10–3000 ppm U; Gieré and Sorensen 2004 and references therein). It has proven to be a successful U–Th–Pb geochronometer, with applications using techniques such as isotope dilution-thermal ionization mass spectrometry (ID-TIMS; e.g., Barth et al. 1994), secondary ion mass spectrometry (SIMS; e.g., Catlos et al. 2000), and laser ablation inductively coupled plasma mass spectrometry (LA-ICP-MS; e.g., Gregory et al. 2007, 2012; El Korh 2014; Smye et al. 2014). Similar to allanite, U and Th are sometimes incorporated into the structure of epidote-clinozoisite, yielding meaningful dates that have been determined through stepwise leaching Pb-Pb dating (Buick et al. 1999), TIMS (Oberli et al. 2004) and LA-ICP-MS (Peverelli et al. 2021). However, the application of U–Th–Pb dating to epidote group minerals has often encountered challenges due to the low concentrations of U-Th, high levels of common (i.e. initial) Pb, excess ^{206}Pb derived from ^{230}Th, and absence of matrix-matched reference materials (Gregory et al. 2007; Smye et al. 2014; Peverelli et al. 2021). These limitations have constrained the broader utilization and accuracy of the epidote-clinozoisite-allanite U–Th–Pb chronometer.

In addition to Th and U, most epidote group minerals can incorporate variable amounts of REEs during crystallisation, particularly in allanite (Frei et al. 2004; Gieré and Sorensen 2004). These REE-rich epidote group minerals have great potential as Lu–Hf geochronometers, and theoretically, meaningful geochronological data can be obtained using the recently developed in situ Lu–Hf method (Simpson et al. 2021). The collision/reaction cell technology is capable of separating ^{176}Lu from ^{176}Hf and resolving isobaric interferences, and thus in situ Lu–Hf geochronology opens a new window for direct and rapid dating of multiple minerals (e.g., garnet, apatite, xenotime, fluorite and calcite) within petrographic context. It has been proven that precise Lu–Hf geochronological constraints can be obtained from minerals with low concentrations of Lu (several ppm to sub-ppm) (Simpson et al. 2021; Glorie et al. 2022a, b, 2023a, b). Lutetium–Hf down-hole fractionation is absent during the laser ablation, and minerals with similar ablation characteristics (e.g., garnet, apatite and xenotime) give similar age off-sets (Simpson et al. 2021). As a result, the correction of Lu–Hf isotope ratios is less dependent on the matrix-matched reference materials. For instance, accurate fluorite Lu–Hf dates were obtained by Glorie et al. (2023b) using a calcite reference material to correct the $^{176}Lu/^{177}Hf$ isotope ratios given their similar ablation characteristics. Furthermore, Lu–Hf and U–Pb isotopic systems in the same mineral may display differences in robustness to thermal disturbance (e.g., apatite and fluorite; Glorie et al. 2023a, b), and thus Lu–Hf geochronology of epidote group minerals may record a different geological history that complements U–Th–Pb geochronology. However, the feasibility and validity of utilizing epidote group minerals for Lu–Hf geochronology have yet to be established. In this study, we present the first Lu–Hf dating of epidote group minerals, including allanite, epidote and clinozoisite, sampled from diverse geological environments, and compare the results with age constraints from other geochronometers. The

Lu–Hf ages were determined using LA-ICP-MS/MS, following a protocol akin to that employed for garnet Lu–Hf dating (Simpson et al. 2021; Brown et al. 2022; Tamblyn et al. 2022). Our findings demonstrate that in situ epidote group minerals Lu–Hf geochronology can indeed yield meaningful ages for low- to intermediate-grade metamorphism, magmatism, mineralisation, and hydrothermal alteration, and can reveal historical information not captured by other dating minerals.

Geological background and sample description

Sampling strategy

Precambrian rocks are the priority targets for the purpose of this research as they have greater radiogenic Hf accumulation and thus potential higher $^{176}Hf/^{177}Hf$ ratios (Simpson et al. 2021). Rocks from different geological settings are selected to cover various epidote group minerals. Clinozoisite sample is from the largest and best-preserved Archean anorthosite complex in SW Greenland, which has been reported to contain clinozoisite from hydrothermal alteration (Polat et al. 2009, 2010). Magmatic allanite samples include the previously studied allanite U–Pb reference material LE40010 from SW Greenland (Smye et al. 2014; Yang et al. 2022), and allanite from Paleoproterozoic pegmatite-hosted REEs deposit/prospect in central China (Zheng et al. 2020; Zhang et al. 2022, 2023; Wei et al. 2023). These allanite samples also have published U–Pb geochronology that can be used for comparison. Metamorphic allanite is sampled from the extensively investigated Strangways Metamorphic Complex, Central Australia (Hand and Sandiford 1999; Mawby et al. 1999; Möller et al. 1999; Scrimgeour and Raith, 2001; Raimondo et al. 2014; Fournier et al. 2016), where allanite occurs as abundant accessory phase throughout the matrix and inclusions in garnet porphyroblasts of metamafic rocks (Bendall 2000). Epidote samples are from Xikuangshan IOCG deposit, SW China (Zhou et al. 2014) and drill holes with porphyry-style alteration in Coompana Province, Australia (Jagodzinski et al. 2019). Timing of their mineralisation and alteration are poorly constrained and thus epidote Lu-Hf system may provide direct geochronological constraints. One additional magmatic allanite sample comes from the monzogranite with porphyry-style alteration in Coompana Province. Detailed geological settings and sample description are introduced below and summarized in Table S1.

Anorthosite complex, SW Greenland

The Archean craton in SW Greenland represents a section of the North Atlantic Craton (NAC, Fig. 1A), consisting of six arc-generated blocks from north to south, named Maniitsoq, Fiskefjord, Sermilik, Bjørnesund, Kvanefjord, and Ivittuut (Windley and Garde 2009). The suturing of these crustal blocks is suggested to have formed by accretion and collision controlled by a series of SE-dipping subduction zones associated with granulite-facies and upper amphibolite-facies metamorphism (Dziggel et al. 2014; Dyck et al. 2015). The final assembly time of the NAC was marked by the injection of the c. 2.72 Ga "Qaarusuk dyke" (Baadsgaard and McGregor 1981), the c. 2.55 Ga Qôrqut Granite Complex (Næraa et al. 2014) and the more recently identified c. 2.56 Ga granulite-facies metamorphism (Dyck et al. 2015). During the Paleoproterozoic, numerous dyke swarms of various orientations and ages have emplaced across the NAC, predominately around c. 2.5 Ga, 2.37 Ga, 2.22 Ga and 2.05–2.03 Ga, respectively (Nilsson et al. 2013).

Anorthosite layered complexes are widespread in the Archean Craton of SW Greenland while only the Fiskenæsset Complex in the Bjørnesund block and the Naajat Kuuat Complex in the Sermilik block have been intensively investigated (Fig. 1A; Myers 1985; Polat et al. 2009, 2010; Hoffmann et al. 2012 and references therein). The Archean anorthosite complexes comprise thick layers of anorthosite, leucogabbro, gabbro, and ultramafic rocks. Their primary stratigraphic units, from bottom to top, include Lower Gabbro, Ultramafic, Lower Leucogabbro, Middle Gabbro, Upper Leucogabbro, Anorthosite, and Upper Gabbro (Myers 1985). Rocks from the Fiskenæsset Complex have provided a Sm–Nd errorchron age of 2973 ± 28 Ma (MSWD = 33) and regression of Pb isotope data defines a date of 2945 ± 36 Ma (MSWD = 44), representing the emplacement of Fiskenæsset Complex in an intra-oceanic island arc (Polat et al. 2010). Similar age of c. 2985 Ma was obtained by Lu–Hf or Sm–Nd isochron regression lines from the Naajat Kuuat Complex (Hoffmann et al. 2012). Subsequently, the Fiskenæsset complex was intruded by tonalite, trondhjemite, and granodiorite (TTG) sheets, which have now metamorphosed to orthogneisses, at c. 2950 Ma (Myers 1985; Polat et al. 2009, 2010). TTGs sampled around the Naajat Kuuat Complex were dated by U–Pb zircon geochronology at c. 2800 Ma (Hoffmann et al. 2012). The metamorphosed anorthosite complexes and adjacent orthogneisses are intruded by muscovite granite sheet at 2660 ± 20 Ma (Pidgeon and Kalsbeek 1978) and mafic dyke swarms around c. 2.37 Ga and c. 2.05–2.03 Ga (Nilsson et al. 2013).

Sample 207824 is a garnet anorthosite from the northernmost part of the Sermilik block (position 64°12′41.76″

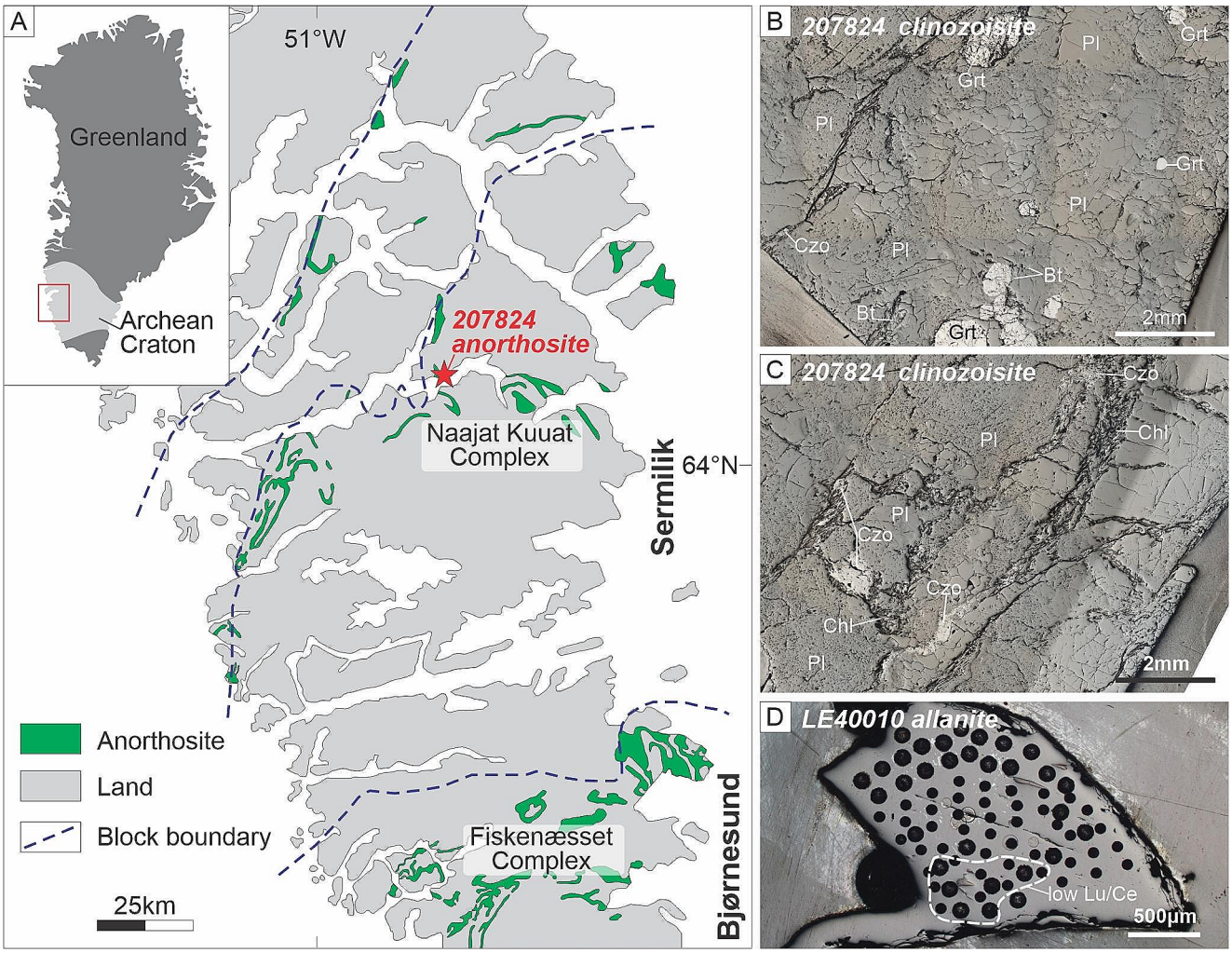

Fig. 1 (**A**) Simplified geological map of the Naajat Kuuat and Fiskenæsset anorthosite complexes from SW Greenland (modified after Hoffmann et al. 2012). (**B** and **C**) Microphotographs of sample 207824, clinozoisite- and chlorite- bearing veins intersect the plagioclase and garnet grains or develop along their boundaries, reflected light. (**D**) Microphotograph of allanite shard of sample LE40010, reflected light, portion with low Lu/Ce ratios are circled by dashed line. Mineral abbreviations are from Whitney and Evan (2010)

N; 50°22′6.24″ W), and thus located close to the Naajat Kuuat Anorthosite Complex and the c. 2.55 Ga Qôrqut Granite Complex (Fig. 1A; Hoffmann et al. 2012; Næraa et al. 2014). The sample closely resembles the garnet anorthosite described by Polat et al. (2009, 2010). It is composed of plagioclase (~95%), garnet and biotite, with irregular clinozoisite-chlorite veins (Fig. 1B and C). Clinozoisite-bearing veins intersect the plagioclase and garnet grains or develop along their boundaries. These veins are typically colourless, but easily discernible under reflected light (RL). Clinozoisite is interpreted to be formed by hydrothermal alteration of plagioclase (Polat et al. 2010), but there is currently no age constraint available for the hydrothermal alteration. The presence of garnet in these rocks has been attributed to the potential contamination of anorthositic magma by basaltic flows, a hypothesis yet to be verified (Windley and Smith 1974).

Sample LE40010 is a dark-brown allanite shard (Fig. 1D) separated from a megacryst (~2 cm long and ~1 cm wide). This megacryst is hosted within a quartz pegmatite from the Fiskenæsset anorthosite complex, and was collected by B.F. Windley in 1950. Detailed petrology of sample LE40010 has been described by Smye et al. (2014). Allanite LE40010 has undergone post-crystallisation hydrothermal alteration, exhibiting heterogeneous zonation in backscattered electron (BSE) images and cracks containing inclusions of thorite and uraninite. This sample was initially analysed using ID-TIMS and yielded a weighted mean $^{207}Pb/^{235}U$ age of 2646 ± 94 Ma and a $^{206}Pb/^{238}U$ age of 2735 ± 226 Ma (Smye et al. 2014). More recently, a relatively homogeneous shard of LE40010 was analysed in situ by LA-(MC)-ICP-MS, producing a lower intercept age of 2613 ± 43 Ma on a Tera-Wasserburg plot and a ^{207}Pb-corrected $^{206}Pb/^{238}U$ age of 2654 ± 63 Ma (Yang et al. 2022).

Huayangchuan uranium-polymetallic deposit, Qinling Orogen, China

The Qinling Orogen, Central China, consists of four distinct tectonic units from north to south, including the southern margin of North China Craton (SNCC), North Qinling, South Qinling, and the northern margin of the Yangtze Block (Chen and Santosh 2014). The Huayangchuan U-polymetallic deposit, along with the adjacent Huangjiagou pegmatite, is situated in the Xiaoqinling district within the SNCC (Fig. 2A). Huayangchuan and Huangjiagou are nestled between the Mesozoic Laoniushan and Huanshan granitic batholiths (Fig. 2B). The predominant stratigraphy in the Xiaoqinling district comprises the Taihua Supergroup, intruded by multiphase magmatism including the Archean Wengchapu TTG gneiss, Proterozoic monzogranite, granite porphyry and pegmatite dikes, Triassic carbonatite dikes, and Jurassic-Cretaceous granitoids. Detailed geological descriptions of the Huayangchuan deposit and Huangjiagou pegmatite can be found in Zheng et al. (2020), Zhang et al. (2022, 2023), and Wei et al. (2023).

Pegmatite-hosted REE mineralisation marks the initial mineralisation phase at Huayangchuan (Zheng et al. 2020). Allanite is the dominant REE ore mineral within the pegmatite. It can be up to centimetres in size and easily identified as dark-brown elongated grains with

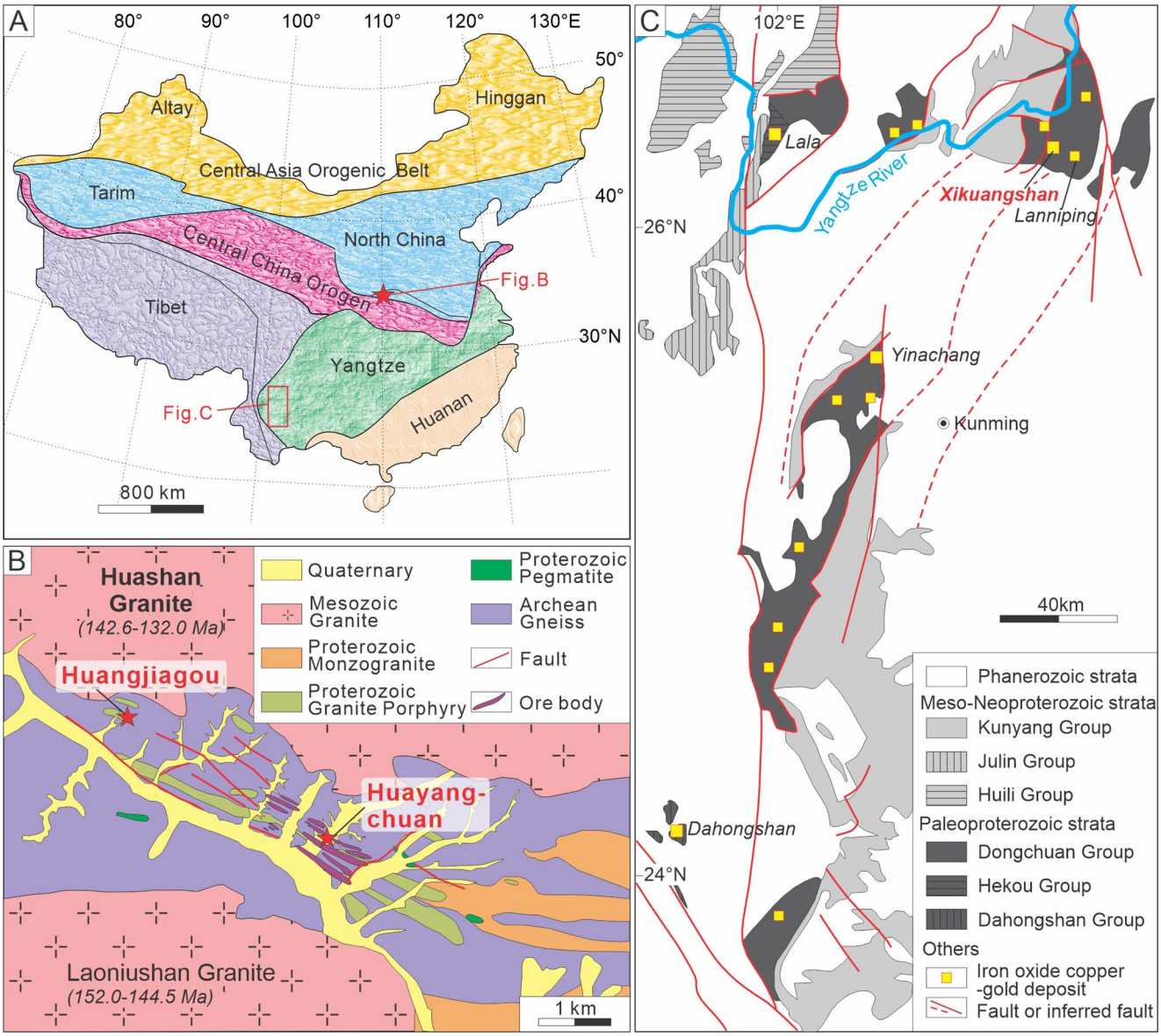

Fig. 2 (**A**) Simplified geological map of China, showing the location of Huayangchuan, Huangjiagou and Kangdian region. (**B**) Simplified geological map of the Huayangchuan uranium-polymetallic deposit and Huangjiagou pegmatite, modified from Zheng et al. (2020). (**C**) Simplified geological map of Kangdian IOCG Province showing location of the Xikuangshan deposit, modified after Su et al. (2021)

reddish radiation-damaged rims. **Sample HYC** is allanite separated from the Proterozoic pegmatite at Huayangchuan, which petrology has been described by Zheng et al. (2020). It displays heterogeneous BSE brightness and cracks crosscutting the grains (Fig. 3A), implying the effect of post-crystallisation hydrothermal alteration. The Proterozoic pegmatite comprises coarse-grained (up to several centimeters) K-feldspar (60–70%), quartz (30–35%) and minor biotite, with accessory minerals of allanite, apatite, titanite and zircon (Zheng et al. 2020). The pegmatite has been dated to be 1807 ± 14 Ma, 1826 ± 8 and 1829 ± 11 Ma by zircon U–Pb geochronology (Yang et al. 2019; Li et al. 2023). Similar pegmatites across the Xiaoqinling district are interpreted as products of the partial melting of the metamorphic basement during the late Paleoproterozoic (~ 1.8 Ga; Zhao et al. 2015). Major mineralisation at Huayangchuan is hosted in Triassic carbonatite dykes (0.01–1 m) that commonly crosscut the early Archean gneiss, TTG suite, and the Proterozoic pegmatite. Its mineralisation time is constrained by titanite and monazite U–Pb geochronology to be 212.3 ± 6.4 Ma and 211.8 ± 5.0 Ma, respectively (Wei et al. 2023).

Huangjiagou pegmatites are discovered in the west of the Huayangchuan ore district (Fig. 2B). They contain granitic mineral assemblages (quartz, K-feldspar, and biotite; Fig. 3B) and a complex accessory mineral assemblage including allanite, zircon, thorite, titanite, betafite, uraninite, brannerite, ilmenite, magnetite, pyrite, galena, calcite, monazite and apatite (Zhang et al. 2022, 2023; Fig. 3B–F). Zircons from Huangjiagou pegmatites yield a weighted mean $^{207}Pb/^{206}Pb$ age of 1826 ± 11 Ma and magmatic allanite yields a lower intercept age of 1829 ± 23 Ma on the Tera-Wasserburg plot and a weighted mean $^{208}Pb/^{232}Th$ age of 1840 ± 17 Ma (Zhang et al. 2022). A younger U–Pb age of 1752 ± 32 Ma obtained from allanite is interpreted to represent post-crystallisation high-temperature metamorphism or hydrothermal metasomatism (Zhang et al. 2023). The pegmatites underwent a secondary phase of metasomatism, characterised by epidotization, biotite veins, and celestite-quartz-calcite crystal caves (Zhang et al. 2023). **Samples HJG-85, HJG-89 and HJG-90** (Fig. 3B–F) are allanite-bearing pegmatites with varying degrees of metasomatism, and two types of allanite could be identified. Type I allanite is magmatic in origin, euhedral to subhedral, and interlocking with quartz, K-feldspar and biotite (Fig. 3B). Type I allanite coexists with zircon, titanite and apatite (Fig. 3C and D). In BSE images, it displays heterogeneous zonation with a brighter core surrounded by darker rim. Type II allanite is hydrothermal in origin and forms aggregates along the calcite-quartz veins during the later metasomatism (Zhang et al. 2023). Type II allanite is normally

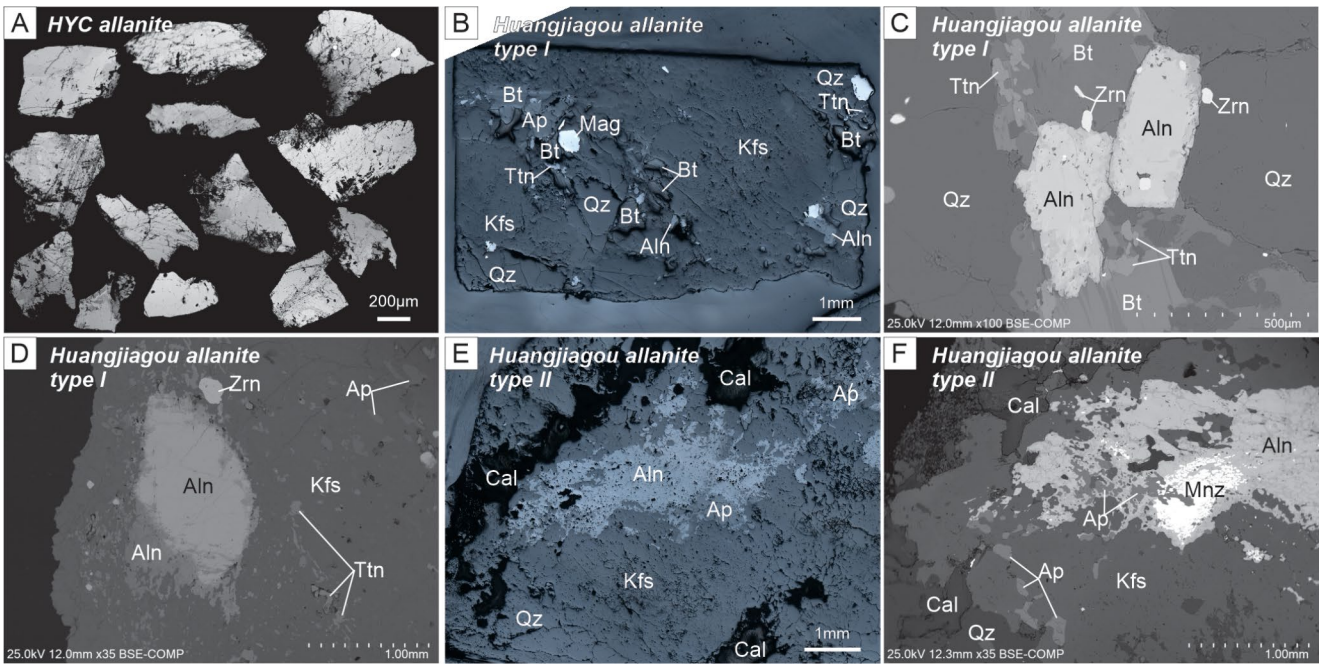

Fig. 3 (**A**) BSE image for allanite from Huayangchuan. HYC allanite grains display heterogeneous brightness and cracks. (**B**) Microphotograph of the type I allanite hosted within pegmatite, reflected light. Pegmatite consists of K-feldspar, quartz and biotite, with accessory minerals of allanite, titanite and apatite. (**C** and **D**) BSE images of the type I allanite. Allanite is hosted in pegmatite together with zircon, titanite and apatite. Allanite grains consist of homogenously bright core and dark rim. (**E**) Microphotograph of the type II allanite, reflected light. Allanite forms aggregates along the calcite-quartz veins and intergrows with apatite and monazite. (**F**) BSE image of the type II allanite, monazite and apatite occur as inclusions in allanite aggregates

anhedral, intergrown with titanite and apatite and monazite (Fig. 3E and F). Type II allanite has homogeneous BSE brightness and thin dark rims along the cracks or grain boundaries, and monazite has uniform BSE brightness. Type II allanite and cogenetic titanite yielded similar U–Pb ages of c. 131 Ma. However, it is worth noting that the type II allanite contains abundant common Pb, and all analyses are clustered in the upper left part of the Tera-Wasserburg plot (Zhang et al. 2023).

Xikuangshan Fe-Cu deposit, Kangdian IOCG province, China

The Kangdian IOCG province is situated on the southwestern margin of the Yangtze Block (Fig. 2A and C; Zhao and Zhou 2011; Zhou et al. 2014). Widespread Paleoproterozoic strata crop out along NS- and NNE-trending faults, including the *Dongchuan* (1742–1716 Ma), *Dahongshan* (1711–1675 Ma), and *Hekou* (1722–1669 Ma) *Groups*, acting as the major host rocks for Fe–Cu deposits. The sediments consist of weakly metamorphosed siliciclastic, dolomitic and interbedded volcanic rocks, with intrusions of coeval 1736–1655 Ma bimodal magmatism (Zhao et al. 2010; Zhao and Zhou 2011). The Paleoproterozoic strata are covered by Mesoproterozoic *Kunyang* (1043–995 Ma), *Huili* (1082–1018 Ma), and *Julin Groups* (1050–1043 Ma), which developed in an intracontinental rift setting (Greentree et al. 2006; Chen et al. 2014; Zhu et al. 2016). Corresponding bimodal igneous and volcanic rocks (1072–1023 Ma) are widespread in the Kangdian region (Zhu et al. 2016; Chen et al. 2018). Arc-related gabbros and granites were emplaced during c. 870–760 Ma, followed by sedimentation of late Neoproterozoic dolostones of the *Dengying* and *Doushantuo Formations*.

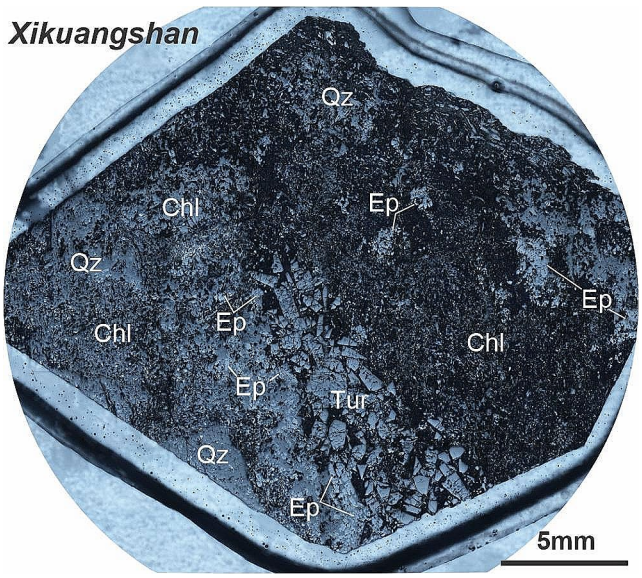

Fig. 4 Microphotograph of the analyzed mount of sample Xikuangshan, reflected light. Tuffaceous host rock has experienced extensive hydrothermalism of quartz, chlorite, epidote and tourmaline. Epidote normally forms aggregates or disseminates as fine grains in quartz or chlorite matrix

All the Kangdian IOCG deposits are hosted in the late Paleoproterozoic strata, including the Dahongshan, Lala, Yinachang, Lanniping and Xikuangshan deposits (Fig. 2C; Zhou et al. 2014). The detailed ore geology, mineralisation styles and hydrothermal alteration zonation are described in Zhao and Zhou (2011) and Zhou et al. (2014). Multiple mineralisation events occurred in the Kangdian IOCG province, mainly at c. 1.7 Ga and c. 1.0 Ga (molybdenite Re–Os; Li et al. 2003; Chen and Zhou 2012; Zhao et al. 2013). The late Paleoproterozoic isotopic ages have been proposed to record the initial Fe-Cu mineralisation events in the region (Zhao and Zhou 2011; Zhao et al. 2013), whereas the Mesoproterozoic ages are interpreted to represent the timing of either hydrothermal remobilisation or an independent mineralisation event (Chen and Zhou 2014; Zhao et al. 2017).

Xikuangshan is a sedimentary rock-hosted stratiform copper deposit, composed of Fe-oxide and Cu-sulfide orebodies hosted in meta-siltstone/meta-tuffaceous rocks of the *Yinmin Formation* of the *Dongchuan Group*. The sedimentary rocks of the *Yinmin Formation* are extensively overprinted by late K-feldspar, sericite, chlorite, quartz, epidote, tourmaline and carbonate. Widespread multi-phase breccias are closely associated with orebodies (Zhou et al. 2014). The geochronological framework of Xikuangshan is poorly constrained at present. Zircon from metatuff layers in the host rock of nearby Yinmin deposit yielded a U–Pb age of 1742 ± 13 Ma (Zhao et al. 2010), and the orebodies are crosscut by dolerite dike of 1701 ± 28 Ma (Zhao et al. 2010, 2013). Chalcopyrite at Xikuangshan yielded Re–Os model ages ranging from c. 1842 Ma to 861 Ma (Li, 2013). Allanite from the nearby Lanniping deposit revealed multiple mineralisations and overprinting at 1728 ± 40 Ma, 1015 ± 66 Ma, and 800 ± 32 Ma (Su et al. 2021). **Sample Xikuangshan** is a metatuffaceous host rock of the *Yinmin Formation*. It has experienced extensive hydrothermalism of quartz, chlorite, epidote and tourmaline (Fig. 4). The rock is dominated by quartz and fine-grained chlorite. Epidote grains are light green in handspeciman, euhedral to subhedral, ranging from 10 to 1000 μm. Epidote normally form aggregates or disseminates as fine grains in quartz or chlorite matrix.

Yambah shear zone, central Australia

The Arunta Inlier (Fig. 5A and B) is a large metamorphic complex that records the last major tectonic event in central

Australia, the Alice Springs Orogeny (450–300 Ma; Hand and Sandiford 1999; Raimondo et al. 2014). The onset of intraplate compressional deformation during the Alice Springs Orogeny (Fig. 5B) is constrained by (1) Sm–Nd isochron dates of 449 ± 10 Ma from upper amphibolite-facies Harts Range Detachment Zone (Mawby et al. 1999), (2) zircon U–Pb dates of 443 ± 6 Ma, recorded in the staurolite-bearing Edwards Creek Shear Zone (Möller et al. 1999), and (3) a monazite U–Pb date of 445 ± 5 Ma and garnet amphibolite Sm–Nd isochron date of 434 ± 6 from the Entire Point Shear Zone mylonites (Scrimgeour and Raith, 2001). During the Devonian–Carboniferous (c. 380–320 Ma), the Strangways Range Complex in the Arunta Inlier experienced diachronous high-strain deformation and fluid infiltration (Fournier et al. 2016).

The Yambah Shear Zone is an amphibolite-facies schist zone transecting adjacent interlayered mafic, felsic and metapelitic granulite-facies rocks of the Strangways Range Complex. Detailed geology of the Yambah Shear Zone is introduced in Bendall (2000) and Fournier et al. (2016). The shear zone is dominated by coarse-grained muscovite-biotite-quartz schists which can also include kyanite, staurolite and/or garnet. The shear zone also contains mafic amphibolites and minor calc-silicate units, composed of hornblende-plagioclase-quartz ± garnet ± staurolite, chlorite-biotite-garnet and diopside-garnet-epidote assemblages respectively. The schists are interpreted to be derived from

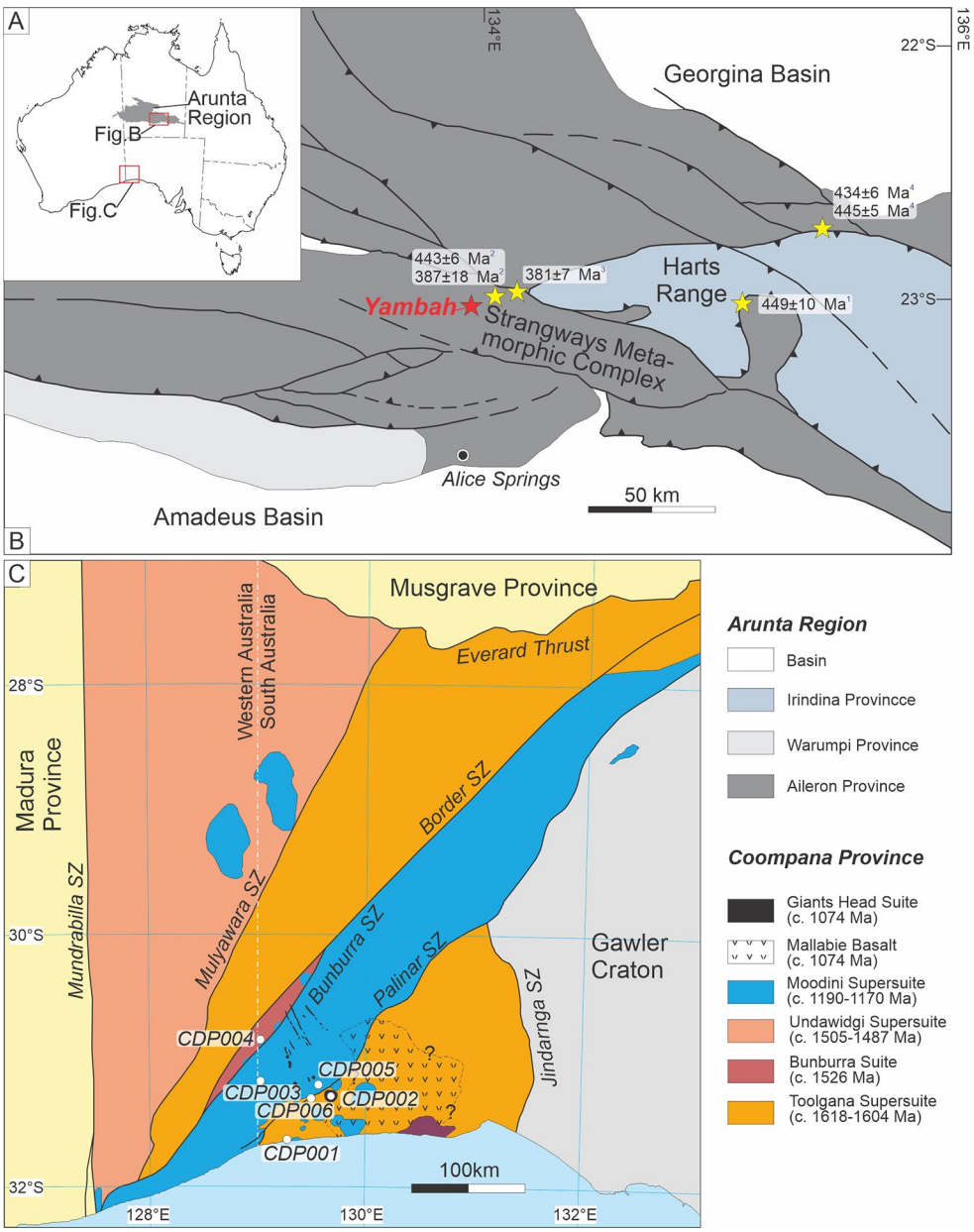

Fig. 5 (**A**) Simplified geological map of Australia, showing the location of Arunta Inlier and Coompana Province. (**B**) Simplified geological map of the Harts and Strangways Metamorphic Complexes in the Arunta Inlier showing the location of Yambah Shear Zone, modified after Fournier et al. (2016). The published geochronological data are from (1) Mawby et al. (1999); (2) Möller et al. (1999); (3) Ballèvre et al. (2000) and (4) Scrimgeour and Raith (2001). (**C**) Simplified geological map of Coompanan Province, modified after Pawley et al. (2020a)

the adjacent Strangways-aged granulites (c. 1730–1690 Ma; Claoué-Long et al. 2008) as individual granulite layers can be traced into their equivalent schist unit (Bendall 2000). Mafic amphibolites from the Yambah Shear Zone produce a spread of Sm–Nd isochron dates from c. 401 Ma to 379 Ma (Bendall 2000), consistent with the Sm–Nd isochron date of 381 ± 7 Ma from the West Bore Shear Zone (Ballèvre et al. 2000) and the monazite U–Pb date of 387 ± 18 Ma from Edwards Creek Shear Zone (Möller et al. 1999) in the Strangways Metamorphic Complex (Fig. 5B). Thermobarometry and phase equilibria studies indicate the mid amphibolite-facies assemblages in the Yambah Shear Zone developed during clockwise prograde metamorphism at conditions of 6 kbar, 600 °C during the Alice Springs Orogeny (Bendall 2000).

Sample Yambah is a coarse-grained chlorite–garnet–allanite–orthoamphibole–biotite-bearing schist (Fig. 6). Garnet in this rock occurs as euhedral porphyroblasts (to 15 mm), forming about 30% of the rock. Garnet contains inclusions of allanite, ilmenite, quartz and apatite (Fig. 6A and B). Chlorite is the dominant phase in the rock, comprising about 60% of the rock, and defines the strong fabric (Fig. 6C). Allanite (100–500 μm), apatite (100–2000 μm), needle-like ilmenite, and minor monazite and xenotime occur throughout the matrix and along the chlorite-defined foliation. Allanite grains are euhedral and form foliation parallel to the chlorite. They have homogeneous BSE brightness. Locally apatite and monazite form cystic aggregates wrapped by the chlorite matrix. Orthoamphibole occurs as euhedral grains within the chlorite dominated foliation (Fig. 6D), and also locally as inclusions within garnet that define curviplaner inclusion patterns.

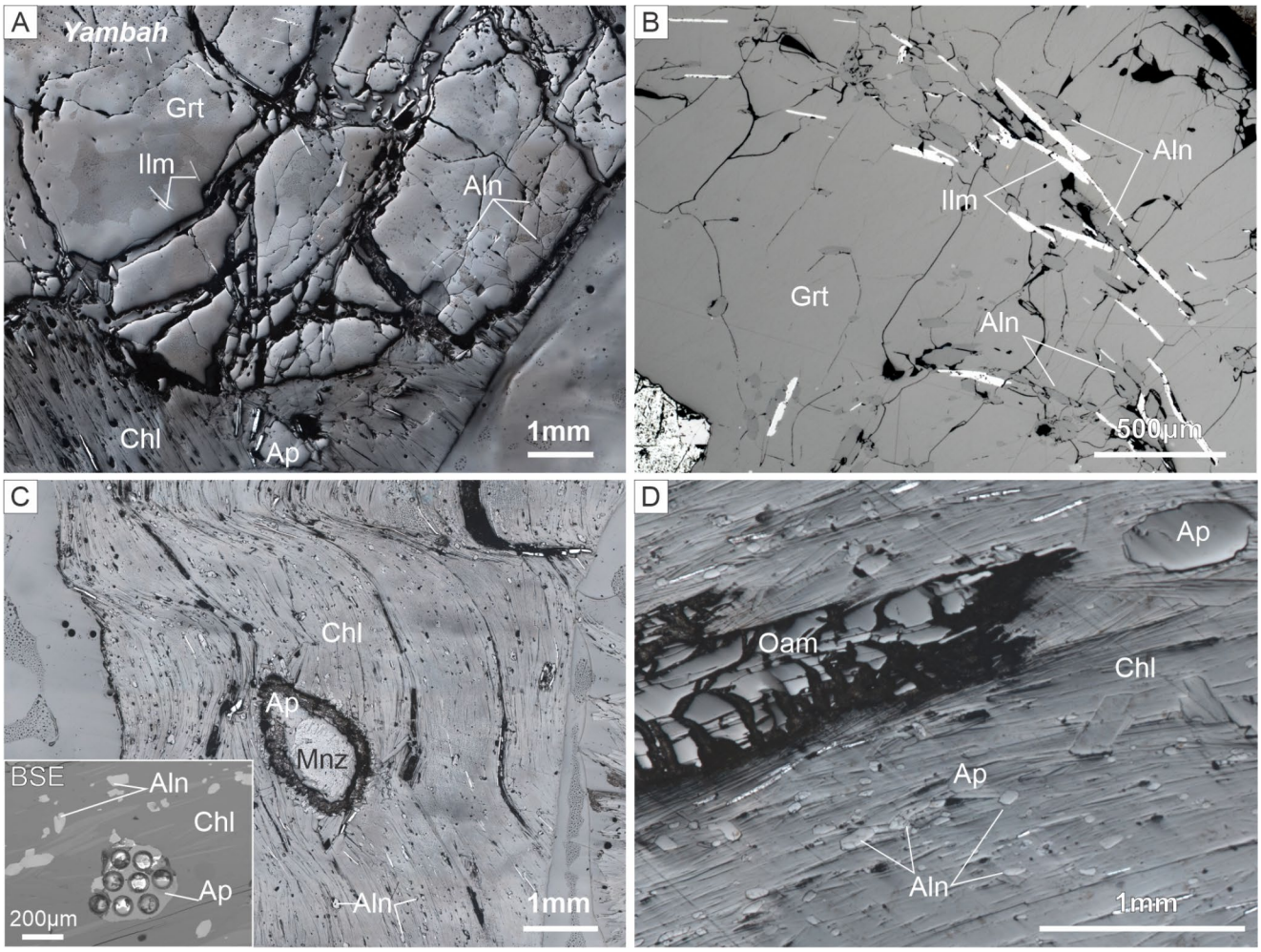

Fig. 6 Microphotographs of the sample Yambah, reflected light. (**A** and **B**) Coarse-grained garnet is wrapped by chlorite fabrics, and ilmenite and allanite occur as inclusions in garnet porphyroblast. (**C**) Allanite disseminates in the chlorite fabrics, and apatite and monazite form cystic aggregates wrapped by the chlorite matrix. (**D**) Minor orthoamphibole is surrounded by the chlorite fabrics, and allanite and apatite are disseminated in the chlorite fabrics

Coompana Province, Australia

The Coompana Province is a completely buried crustal block that occurs at the junction of the West, South and North Australian cratons (Fig. 5A and C). The basement geology of the Coompana Province used to be poorly known due to the lack of outcrops and our understanding of this Province has been greatly enhanced by the recent Coompana Drilling Project, including 8 drill holes (CDP001 to CDP008; Pawley et al. 2018; Wise et al. 2018; Jagodzinski et al. 2019).

The oldest rocks are the c. 1618 Ma Toolgana Supersuite intersected in drill holes CDP001 and CDP006. They are similar in age and geochemistry to the c. 1647–1608 Ma St Peter Suite in the Gawler Craton (Symington et al. 2014; Reid et al., 2019) and are interpreted to represent the subduction and arc magmatism outboard of the Gawler Craton (Kirkland et al. 2017; Hartnady et al. 2020). Geophysical datasets suggest these rocks are common throughout the Coompana Province, defining the NNE-trending grain prominent on aeromagnetic and gravity datasets (Pawley et al. 2020a). Following the cessation of arc-related magmatism at c. 1526 Ma (i.e., Bunburra Suite), the A-type Undawidgi Supersuite developed during intracontinental extension during c. 1505–1487 Ma (Dutch 2018; Wise et al. 2018). From c. 1200–1070 Ma, the Coompana Province underwent two stages of intraplate magmatism, including the 1190–1140 Ma Moodini Supersuite granitoids and the c. 1074 Ma mafic Giants Head Suite (Jagodzinski et al. 2019; Pawley et al. 2020a; Spaggiari et al. 2020). The Moodini Supersuite granitoids are strongly magnetic and form a NE-trending belt of overlapping plutons within a shear-bounded corridor (Pawley et al. 2020a). The Moodini Supersuite magmatism was contemporaneous with widespread crustal anatexis, with metamorphism constrained at c. 1163 Ma (Jagodzinski et al. 2019). The Giants Head Suite includes mafic intrusive and extrusive rocks interpreted to form part of the c. 1075 Ma Warakurna Supersuite (Pawley et al. 2020b).

Sample 4381386 is allanite-bearing monzogranite sampled from the depth of 532.19–532.28 m in drill hole CDP004 (Fig. 7A). The allanite-bearing monzogranite belongs to the Moodini Supersuite and crosscuts the Undawidgi Supersuite, having gradational boundaries with the surrounding rocks. It is reddish brown-grey, fine- to medium-grained and equigranular. It is composed of plagioclase, K-feldspar and quartz, minor biotite and accessory minerals allanite, titanite, apatite and zircon. A single allanite grain (3.5 mm×1 mm) is hosted in plagioclase and contacts with biotite and quartz. The sample has experienced

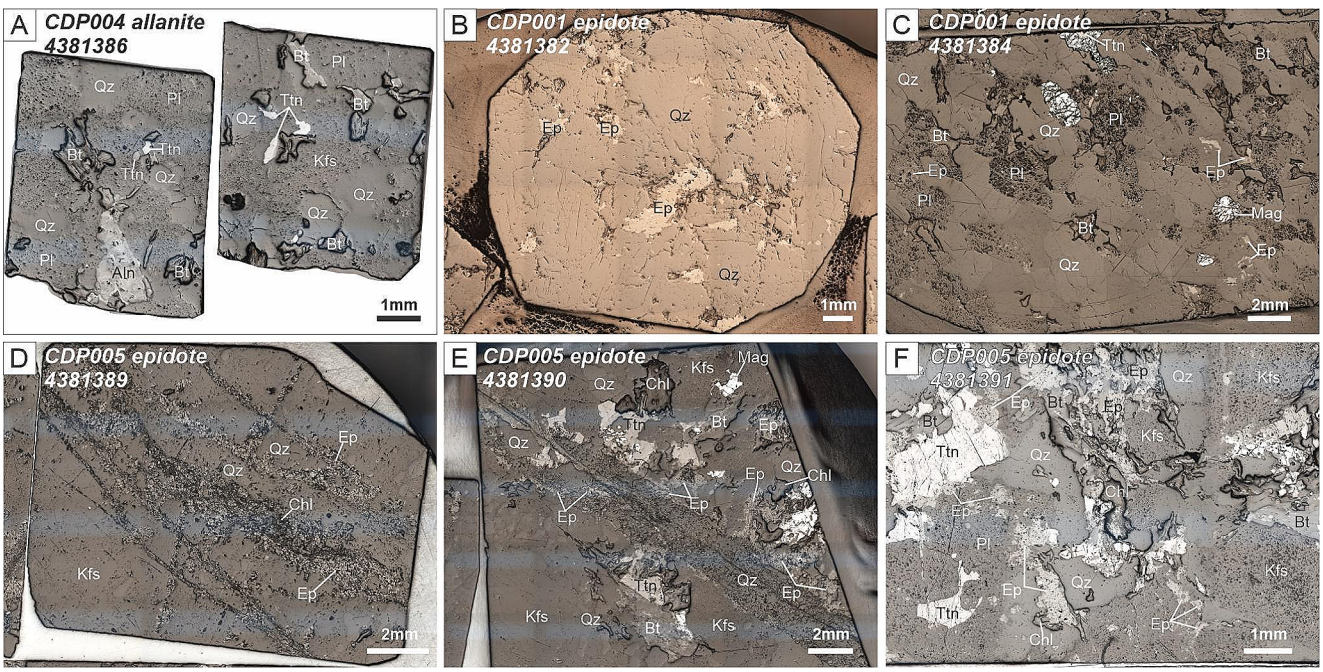

Fig. 7 Microphotographs of sample from Coompana Province, reflected light. (**A**) Sample 4,381,386 from drill hole CDP004, allanite intergrows with quartz, plagioclase and biotite. Titanite occurs as accessory mineral in the monzogranite. (**B**) Sample 4,381,382 from drill hole CDP001, epidote occurs in quartz vein crosscutting the altered monzogranite. (**C**) Sample 4,381,384 from drill hole CDP001, plagioclase is partially altered to epidote in the monzogranite. Titanite occurs as accessory mineral. (**D**) Samples 4,381,389 from drill hole CDP005, epidote-chlorite veins/veinlets crosscut the granite. (**E**) Sample 4,381,390 from drill hole CDP005. Granite is crosscut by quartz-epidote veins. Plagioclase grains are partially altered to epidote and biotite is partially altered to chlorite. (**F**) Sample 4,381,391 from drill hole CDP005, granite is altered by epidote and chlorite. Epidote replaces plagioclase or forms corona outside titanite

post-crystallisation hydrothermal alteration, with epidote locally replacing plagioclase. Previously, a biotite leucomonzogranite from 536.5 to 537.38 m and a foliated dark green quartz-syenite from 674.35 to 676.57 m yielded zircon U–Pb dates of 1197 ± 12 Ma and 1174 ± 9 Ma, respectively (Jagodzinski et al. 2019). More recently, an apatite Lu–Hf date was obtained of 1195 ± 35 Ma (Bedoya et al. 2024).

Samples 4381382 and 4381384 are sampled from depths of 448.27–448.37 m and 501.58–501.7 m in drill hole CDP001 (Fig. 7B and C). They are medium-grained massive monzogranite of the Moodini Supersuite that intruded into the migmatitic rocks of the Toolgana Supersuite. The monzogranite is composed of K-feldspar, plagioclase, quartz, and biotite with accessory minerals of titanite, apatite, zircon and allanite. Both samples 4381382 and 4381384 have experienced hydrothermal alteration, with the development of epidote-quartz veins crosscutting the monzogranite (Fig. 7B) or epidote replacing plagioclase (Fig. 7C). Anhedral epidote grains are hosted in quartz veins in sample 4381382 (Fig. 7B). Plagioclase grains in sample 4381384 are greenish but dominated by plagioclase rather than epidote, indicating the incomplete epidotization of plagioclase (Fig. 7C). Previously, zircon U–Pb geochronology of monzogranite at 421.70–423.15 m indicates the monzogranite was derived by the partial melting of the c. 1618 Ma Toolgana Supersuite orthogneiss (Dutch 2018), and emplaced at 1141 ± 15 Ma (Jagodzinski et al. 2019). This is confirmed by apatite Lu–Hf and U–Pb dates of 1154 ± 11 Ma and 1135 ± 16 Ma, respectively (Bedoya et al. 2024).

Samples 4381389, 4381390 and 4381391 are coarse-grained granites sampled from depths of 566.96–567.1 m, 637–637.19 m, and 645.97–646.13 m, respectively, in drill hole CDP005 (Fig. 7D–F). The granite samples are reddish, and composed of K-feldspar, plagioclase, quartz, biotite, and accessory minerals of titanite, apatite and zircon. The samples are characterized by extensive hydrothermal alteration of albite, sericite, chlorite, epidote and fluorite (Jagodzinski et al. 2019). Epidote normally replaces plagioclase or occurs in the epidote-chlorite-quartz veins crosscutting the coarse-grained granite. Coarse-grained titanite is subhedral to euhedral and interlocks with plagioclase, quartz and biotite or occurs as inclusions in plagioclase. Titanite is enclosed by epidote-chlorite or crosscut by epidote-quartz veins (Fig. 7E and F), indicating the development of epidote alteration is later than the titanite crystallisation. Granite sampled at 478.14–479.96 m yielded consistent zircon U–Pb, apatite Lu–Hf and apatite U–Pb dates of 1148 ± 7 Ma, 1164 ± 16 Ma and 1149 ± 16 Ma, respectively, representing the timing of magmatic crystallisation (Jagodzinski et al. 2019; Bedoya et al. 2024).

Analytical methods

All samples were mounted in 2.5 cm diameter epoxy mounts, and RL or BSE images were obtained to reveal the petrogenetic context of the analysed epidote group minerals.

Lu–Hf geochronology and trace elements

Lu–Hf geochronology and trace elements analyses of epidote group minerals, garnet and apatite were conducted at Adelaide Microscopy, The University of Adelaide, following a methodology primarily based on Simpson et al. (2021), which we briefly outline here and summarized in Table 1. The Lu–Hf analyses were performed using a RESOlution 193 nm excimer laser ablation system coupled with an Agilent 8900 ICP-MS/MS. NH_3 was employed as the reaction gas, supplied as a mixture of 10% NH_3 in 90% He. Laser beam diameters ranged from 67 to 120 µm for allanite, apatite and garnet, and 173 µm for clinozoisite and epidote. Laser repetition rates of 10 Hz were used to enhance sensitivity. The following isotopes (mass shifts included in brackets) were measured: ^{27}Al, ^{43}Ca, $^{(47+66)}Ti$, ^{57}Fe, ^{88}Sr, $^{(89+83)}Y$, $^{(90+83)}Zr$, $^{(140+15)}Ce$, ^{146}Nd, ^{147}Sm, ^{172}Yb, ^{175}Lu, $^{(175+82)}Lu$, $^{(176+82)}Hf$, $^{(178+82)}Hf$. ^{175}Lu was measured as a proxy for ^{176}Lu, and ^{178}Hf was measured as a proxy for ^{177}Hf. Calculation of ^{176}Lu and ^{177}Hf was conducted assuming stable present-day $^{176}Lu/^{175}Lu$ and $^{177}Hf/^{178}Hf$ ratios, with detailed procedures outlined in Simpson et al. (2021).

LADR (Norris and Danyushevsky 2018) was used as the data reduction software. Background-subtracted isotopic ratios were normalised to NIST-610 glass using the Nebel et al. (2009) ID-MC-ICP-MS isotopic compositions of $^{176}Lu/^{177}Hf = 0.1379 \pm 0.005$ and $^{176}Hf/^{177}Hf = 0.282111 \pm 0.000009$. NIST-610 was analysed every 20–40 unknown samples and further used to correct the isotope ratios for instrument mass bias and drift. Subsequently, a matrix-fractionation correction needs to be conducted on the $^{176}Lu/^{177}Hf$ ratio. Although a reference material with the same matrix as the analysed samples is desirable, it has been shown that the correction factors for materials with similar ablation characteristics (crater depth, ablation rate), analysed with the same analytical conditions, are indistinguishable (Glorie et al. 2023a, b). Here, Högsbo garnet (1029 ± 1.7 Ma; Romer and Smeds 1996) was utilized to correct the matrix-induced fractionation for both the garnets and the epidote group minerals in this study, due to their similar ablation characteristics (Figure S1) and the absence of Lu–Hf downhole fractionation (Simpson et al. 2021, 2022; Glorie et al.

Table 1 Analysis and LA-ICP-MSMS tuning parameters for Lu–Hf analyses

Plasma parameters	
Radio frequency (RF) power	1350 W
Sample depth	4.5 mm
Ar carrier gas	0.96 L min^{-1}
He carrier gas	0.38 L min^{-1}
N_2 addition	4 mL min^{-1}
Lens parameters	
Extract 1	–3.5 V
Extract 2	–145 V
Omega bias	–90 V
Omega lens	9.0 V
Q1 entrance	–10 V
Q1 exit	–2.0 V
Cell focus	–2.0 V
Cell entrance	–130 V
Cell exit	–70 V
Deflect	6.0 V
Plate bias	–90 V
Q1 parameters	
Q1 bias	–1.0 V
Q1 pre–filter bias	–10 V
Q1 post–filter bias	–10 V
Cell parameters	
He flow	1.0 mL min^{-1}
10% HN3 90% He gas flow	3.0 mL min^{-1}
Octopole bias	–2.5 V
Axial acceleration	2.0 V
Octopole RF	–180 V
Energy discrimination	–15 V
Q2 parameters	
Q2 bias	–15 V
Wait time offset	2 ms
Analysis parameters	
Laser wavelength	193 nm
Laser fluence	3.5 J cm^{-2}
Laser spot diameter	67, 120 and 173 µm (43 µm; NIST610 glass)
Laser repetition rate	10 Hz
Washout	30 s (post–cleaning pulse) + 20 s (post analysis)
Background	30 s
Analysis time	40 s
Isotopes measured/dwell times (ms)	^{27}Al (2), ^{43}Ca (2), $^{(47+66)}$Ti (2), ^{57}Fe (2), ^{88}Sr (2), $^{(89+83)}$Y (2), $^{(90+83)}$Zr (2), $^{(140+15)}$Ce (2), ^{146}Nd (2), ^{147}Sm (2), ^{172}Yb (10), ^{175}Lu (10), $^{(175+82)}$Lu (100), $^{(176+82)}$Hf (150), $^{(178+82)}$Hf (150)

2023b). Reference garnet Black Point BP-1 (concordant U-Pb age of 1745 ± 14 Ma, multi-session Lu-Hf age of 1740 ± 7 Ma; Lane, 2011; Glorie et al. 2024) and reference allanite LE40010 (^{207}Pb-corrected ^{206}Pb/^{238}U age of 2654 ± 63 Ma; Yang et al. 2022) were used to verify the accuracy of the calibration procedure. Additionally, some apatite samples were dated by the Lu–Hf method in the same rocks as the epidote group minerals. OD-306 apatite (1597 ± 7 Ma; Thompson et al. 2016) was used to correct the matrix-induced fractionation for apatite and reference apatite Bamble-1 (corrected Lu–Hf age: 1097 ± 5 Ma) was monitored for accuracy checks (Glorie et al. 2022a, b). IsoplotR was used to calculate the inverse isochron ages (Vermeesch 2018). The ^{176}Lu decay constant of 0.00001867 ± 0.00000008 Myr^{-1} (Söderlund et al. 2004) was used for all age calculations. Inverse isochrons were chosen over normal isochrons as they provide a more robust age calculation method for datasets with strong uncertainty correlations (Li and Vermeesch 2021). For samples with insufficient variability in ^{177}Hf/^{176}Hf ratios between individual analyses, unanchored isochron regression cannot robustly constrain the Lu–Hf age. Fortunately, the range of terrestrial initial ^{177}Hf/^{176}Hf ratios is relatively narrow compared to the Lu/Hf ratios typically observed in epidote group minerals. Hence, following Glorie et al. (2023a, 2024), an anchored regression is used to calculate the Lu–Hf age for samples with low ^{177}Hf/^{176}Hf variability. The anchored regression algorithm is detailed in Vermeesch et al. (2024) and the initial ^{177}Hf/^{176}Hf anchor used in this work is 3.55 ± 0.05, which covers the entire range of terrestrial possibilities (Spencer et al. 2020). Trace elements were processed using the glass NIST-610 as a standard, all allanite analyses were assumed to have 6.9 wt% Ca and all epidote-clinozoisite analyses were assumed to have 16.6 wt% Ca. Garnet analyses of Yambah were assumed to have 11.1 wt% Al (probe data in Bendall 2000), and garnet analyses of sample 207,824 were assumed to have 12 wt% Al. All apatite analyses were assumed to have 39.4 wt% Ca.

U–Pb geochronology

LA-ICP-MS monazite and titanite U–Pb analyses were collected on an Agilent 8900 ICP-MS coupled with a RESOlution 193 nm excimer laser ablation system at Adelaide Microscopy, The University of Adelaide. The ablation of monazite was performed with a spot size of 13 µm, a frequency of 5 Hz, and a fluence of 4–5 J/cm^2. The total acquisition time for each analysis was 60 s, including 30 s of background measurement, followed by 30 s of laser ablation. Common lead was not corrected in the age calculations due to unresolvable interference of ^{204}Hg on the ^{204}Pb isotope peak. Mass bias, elemental fractionation, and instrument drift were corrected using the monazite standard MAdel (TIMS normalization data: ^{207}Pb/^{206}Pb age = 492.01 ± 0.77 Ma, ^{206}Pb/^{238}U age = 517.9 ± 2.6 Ma and ^{207}Pb/^{235}U

age = 513.13 ± 0.20 Ma; updated from Payne et al. (2008) with additional TIMS analyses). Data accuracy was monitored by analyses of in-house monazite standard 222 (SHRIMP $^{206}Pb/^{238}U$ age 450.2 ± 3.4 Ma; Maidment 2005) and Ambat ($^{206}Pb/^{238}U$ age c. 520 Ma). Standards were analysed every 12–15 unknown analyses. Titanite grains were ablated with a frequency of 5 Hz, fluence of 3.5 J/cm^2 and a spot size of 43 µm. The acquisition time of each analysis was 70 s, comprising 30 s of background measurement and 40 s of ablation. Titanite U–Pb data were corrected for mass bias, elemental fractionation and instrument drift based on the measured isotopic ratios of the primary titanite reference, MKED-1 (TIMS normalization data: $^{207}Pb/^{206}Pb$ age = 1521.02 ± 0.55 Ma; Spandler et al. 2016). Mt Painter was analysed as a secondary standard to measure data accuracy by standard–sample bracketing every ~ 15 unknown analyses. Data reduction was conducted in LADR (Norris and Danyushevsky 2018) and age calculations were performed in IsoplotR (Vermeesch 2018).

Sm–Nd geochronology

Mineral separates were prepared via magnetic and heavy liquid separation techniques which were also used to remove impurities from the garnet fraction. Surface contamination on the handpicked mineral separates was removed by an ultrasonic cleaner in 1 M HCl solution. A whole-rock fraction of the matrix surrounding the garnets was crushed and milled. Between 125 and 300 mg and 100–150 mg of sample was used for mineral separates and whole rock, respectively. The mineral separates were milled under ethanol in an agate mortar to a fine grain size. To minimize contamination of mineral fractions by REE-rich inclusions, the milled fractions were leached in hot 1 M HF for 1 h. The leachate was pipetted from the residual solid material and the solid material washed in cold 6 M HCl separately to remove any trace of the leachate fraction. For the whole-rock component, around 150 mg of milled whole rock was dissolved in steel jacketed, high pressure Teflon bombs using a HNO_3–HF acid mixture heated to 200 °C for periods of 5 days. All samples were spiked with a mixed ^{147}Sm–^{150}Nd spike prior to dissolution. Nd and Sm isotopic ratios were measured by thermal ionization mass spectrometry (TIMS) on a Finnigan MAT 262 system in static mode at the University of Adelaide. The isotopic ratios were corrected for fractionation to $^{146}Nd/^{144}Nd$ = 0.721903 and to a $^{152}Sm/^{149}Sm$ ratio of 1.9347. Spiked samples of BCR-1 yielded a $^{143}Nd/^{144}Nd$ ratio of 0.512598 ± 17 after spike unmixing. The $^{143}Nd/^{144}Nd$ reproducibility of the internal standard over the course of the study (n = 10) was 0.511602 ± 0.00001. For age calculations Sm/Nd errors were estimated to be ± 0.3%. Age calculation (reported at 95% confidence) are performed in IsoplotR (Vermeesch 2018) based on a decay constant for ^{147}Sm of (6.524 ± 0.024) × 10^{-12} a^{-1} (Villa et al. 2020). The total procedural Sm and Nd blanks were 100 pg.

Results

All geochronology data is summarized in Table S2–S7, and all ages are reported with 2σ absolute uncertainties.

Anorthosite complex, SW Greenland

Clinozoisite sample 207824 was analysed over two analytical sessions, yielding Lu concentrations of 0.27–28 ppm, $^{176}Lu/^{177}Hf$ ratios between 0.06 and 4.55, and $^{177}Hf/^{176}Hf$ ratios between 2.84 and 3.57. Its Al/(Al + Fe) ratios range from 0.72 to 0.95, confirming the dominance of clinozoisite endmember. Fifty-nine spots have $^{176}Lu/^{177}Hf$ ratios lower than 1, and analyses with $^{176}Lu/^{177}Hf$ ratios higher than 1 normally have higher Lu concentrations of 3.4–28 ppm. All analyses define an inverse isochron Lu–Hf age of 2372 ± 69 Ma (n = 70, MSWD = 1.1; Fig. 8A). Additionally, thirty-eight Lu–Hf analyses of **garnet** yield an inverse isochron age of 2577 ± 15 Ma (n = 38, MSWD = 2.8; Fig. 8B) anchored by an initial $^{177}Hf/^{176}Hf$ ratio of 3.55 ± 0.05. Garnet has Lu concentrations of 73–171 ppm.

Allanite Sample LE40010 was analysed over two analytical sessions. Despite all analyses have relatively uniform trace elements concentrations, e.g., Lu contents of 1.4–1.9 ppm and Ce contents of 50,325–68,919 ppm, the resulting $^{176}Lu/^{177}Hf$ ratios (3.08–6.21) and $^{177}Hf/^{176}Hf$ ratios (2.42–3.01) define two clusters (Fig. 8C). Cluster with lower $^{176}Lu/^{177}Hf$ ratios corresponds to allanite portion with lower Lu/Ce ratios (Figs. 1D and 8C), indicating the allanite shard is not compositionally homogeneous. The clustered $^{176}Lu/^{177}Hf$ ratios and $^{177}Hf/^{176}Hf$ ratios yield unanchored inverse isochron ages with uncertainties of 300–500 Ma and thus an initial $^{177}Hf/^{176}Hf$ ratio of 3.55 ± 0.05 was used to anchor the inverse isochron. Thirty-nine analyses, analysed with a 67 µm laser beam size, in session 2 yielded an inverse isochron Lu–Hf age of 2591 ± 135 Ma (n = 39, MSWD = 0.82; Fig. 8C). Using larger laser spots of 100 µm, twenty-seven analyses from session 3 yield smaller uncertainties and define an inverse isochron Lu–Hf age of 2703 ± 116 Ma (n = 27, MSWD = 0.55). All analyses from the two sessions combined yield an inverse isochron Lu–Hf age of 2660 ± 109 Ma (n = 66, MSWD = 0.77; Fig. 8C).

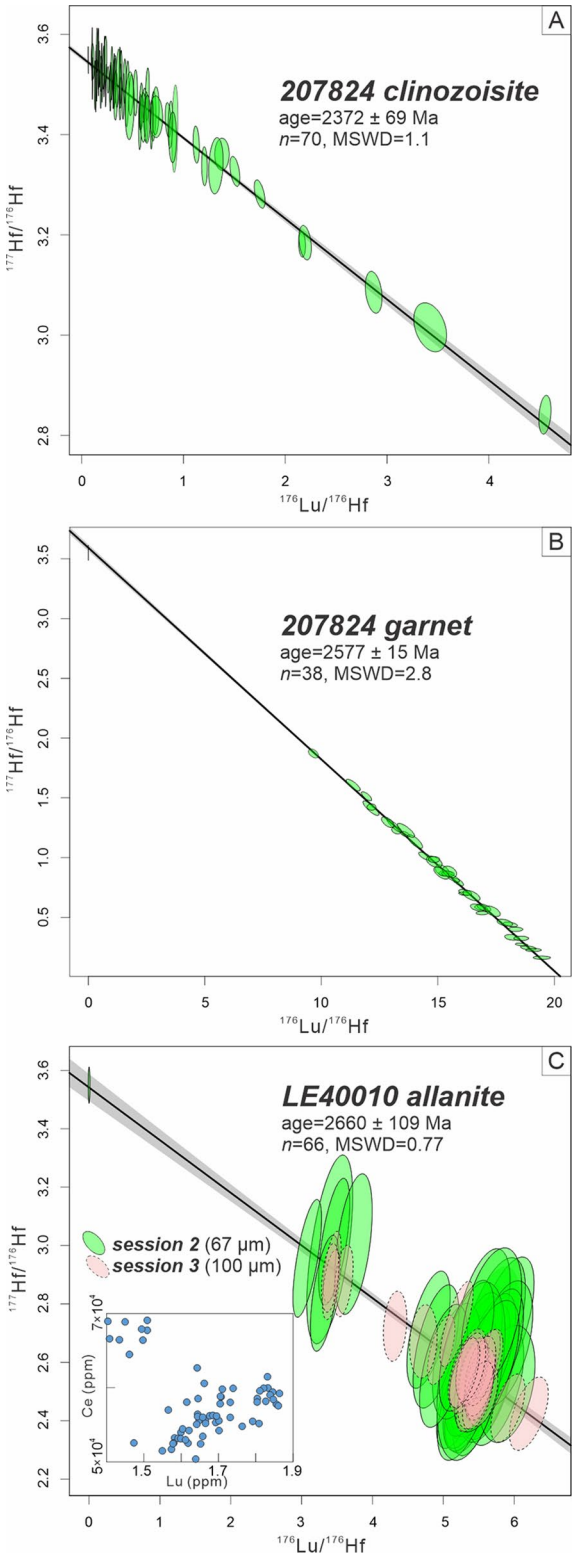

Fig. 8 Lu–Hf inverse isochrons for (**A**) clinozoisite in sample 207,824, (**B**) garnet in sample 207,824 and (**C**) allanite LE40010 from Fiskenæsset anorthosite complex

Huayangchuan uranium-polymetallic deposit, Qinling Orogen, China

Allanite sample HYC was analysed by fifty-seven laser spots over two analytical sessions. The allanite separates yielded very dispersed Lu contents of 4.3–25 ppm, $^{176}Lu/^{177}Hf$ ratios of 7.61–22.11 and $^{177}Hf/^{176}Hf$ ratios of 0.80–2.73. There is a positive correlation between Lu contents and final $^{176}Lu/^{177}Hf$ ratios. Despite the different BSE brightness and zonation of allanite grains, all analyses plot along a single isochron (Fig. 9A). Thirty-six analyses from session 2 define an inverse isochron age of 1812 ± 39 Ma (n = 36, MSWD = 2) anchored by an initial $^{177}Hf/^{176}Hf$ ratio of 3.55 ± 0.05. Twenty-one analyses from session 3 define an identical inverse isochron age of 1810 ± 32 Ma (n = 21, MSWD = 1.5) using the same anchor $^{177}Hf/^{176}Hf$ ratio. However, unanchored inverse isochron ages of 1870 ± 39 Ma and 1854 ± 43 Ma are obtained from two sessions, with initial $^{176}Hf/^{177}Hf$ ratios of 0.2663 ± 0.0051 and 0.2712 ± 0.0057, respectively. The initial $^{176}Hf/^{177}Hf$ ratios are lower than the recommended crustal Hf isotope ratios of ~0.280 – ~0.282 (Spencer et al. 2020; Simpson et al. 2021) and the unanchored Lu–Hf ages are older than the zircon U–Pb ages of the host pegmatite, and thus the anchored inverse isochron ages are preferred.

Allanite samples HJG-85, HJG-89 and HJG-90 contain two types of allanite, corresponding to magmatic (type I) and hydrothermal (type II) stages, respectively. Two types of allanite have distinct geochemistry such as the mobile Sr and immobile Zr concentrations (Fig. 9B). Type I allanite has Sr contents of 63–1289 ppm and Zr contents of 2.8–7.3 ppm while type II allanite has Sr contents of 1767–3217 ppm and Zr contents of 0.25–1.4 ppm. Two types of allanite have comparable REE contents, including 3.1×10^3–8.4×10^4 ppm Ce and 0.23–4.3 ppm Lu in type I allanite and 4.9×10^4–9.6×10^4 ppm Ce and 1.0–3.3 ppm Lu in type II allanite. However, two types of allanite are characterized by different Lu/Hf ratios. Type I allanite from Huangjiagou has $^{176}Lu/^{177}Hf$ ratios that vary between 0.004 and 8.75 and $^{177}Hf/^{176}Hf$ ratios between 2.53 and 3.57, and high $^{176}Lu/^{177}Hf$ ratios correspond to high Lu centration. Seventy-eight analyses define an inverse isochron age of 1821 ± 74 Ma (n = 78, MSWD = 0.83; Fig. 9C). Type II allanite in sample HJG-90 has higher $^{176}Lu/^{177}Hf$ ratios that vary between 8.89 and 69.30, and $^{177}Hf/^{176}Hf$ ratios between 2.45 and 3.60. Forty-four analyses define an anchored inverse isochron age of 215 ± 34 Ma using an initial $^{177}Hf/^{176}Hf$ ratio of 3.55 ± 0.05 (n = 44, MSWD = 1; Fig. 9D).

Monazite and apatite aggregates occur as inclusions in type II allanite in sample HJG-90. Monazite grains are 10–500 µm, and are unzoned in BSE images (Fig. 3F). Thirty

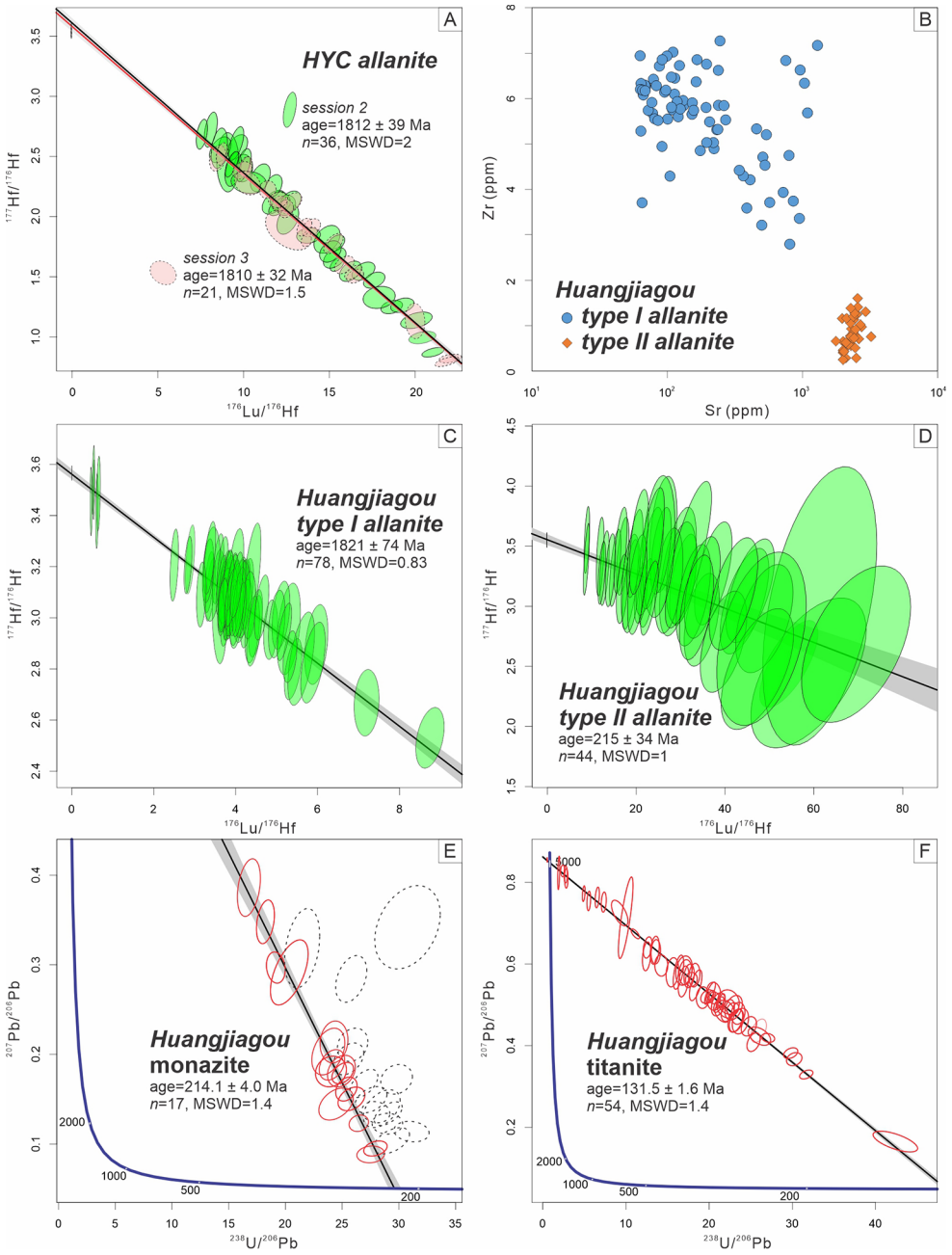

Fig. 9 (**A**) Lu–Hf inverse isochron for sample HYC, including data from two laser sessions. (**B**) Zr vs. Sr plot for two types of allanite at Huangjiagou. (**C**) Lu–Hf inverse isochron for type I allanite at Huangjiagou. (**D**) Lu–Hf inverse isochron for type II allanite at Huangjiagou. (**E**) U–Pb age for monazite inclusions in type II allanite at Huangjiagou, dashed ellipses with potential Pb loss are excluded for age calculation. (**F**) U–Pb age for titanite at Huangjiagou

analyses from monazite are discordant due to the presence of common Pb and Pb loss. Seventeen analyses define an isochron with a lower intercept age of 214.1 ± 4.0 Ma ($n = 17$, MSWD = 1.4, prob. = 0.15; Fig. 9E), representing the crystallisation time of monazite. Analyses from titanite cogenetic with type I allanite in samples HJG-85 and HJG-89 (Fig. 3B–D) are plotted as a single isochron, and they collectively yield a lower intercept age of 131.5 ± 1.6 Ma on the Tera-Wasserburg plot (Fig. 9F).

Xikuangshan Fe-Cu deposit, Kangdian IOCG province, China

Epidote sample Xikuangshan was analysed over two analytical sessions, and epidote grains with higher $^{176}Lu/^{177}Hf$ ratios were targeted during the second session. Epidote Xikuangshan has Al/(Al + Fe) ratios of 0.24–0.78, Ce contents of 24–965 ppm and Lu contents of 0.17–2.1 ppm. The majority of epidote analyses have Lu contents lower than 1 ppm and yielded large uncertainties for the $^{177}Hf/^{176}Hf$ ratios, leading to a significant uncertainty on the calculated

Lu–Hf age. Fifty-two analyses define an inverse isochron age of 1008 ± 103 Ma (n = 52; MSWD = 1.1; Fig. 10).

Yambah shear zone, Central Australia

Allanite, garnet, and apatite were analysed for Lu–Hf geochronology in **sample Yambah**. Both allanite and apatite are distributed evenly throughout the chlorite foliation in the matrix. In addition allanite occurs as inclusions in garnet, indicating that at least some of the allanite predates the growth of garnet. Two hundred and forty-six allanite analyses have dispersed Lu contents of 1.3–23 ppm, $^{176}Lu/^{177}Hf$ ratios of 0.04–98.96 and $^{177}Hf/^{176}Hf$ ratios of 0.76–3.55, and yield an inverse isochron age of 432 ± 7 Ma (n = 246, MSWD = 1.7; Fig. 11A). The majority of allanite contains Lu contents between 10 and 22 ppm, corresponding to higher $^{176}Lu/^{177}Hf$ ratios.

Three ~ 1 cm **garnet** grains were analysed from **sample Yambah**. During the analysis, spots from both cores and rims were analysed to cover areas with different Lu concentrations and Lu/Hf ratios. Care was taken to avoid hitting allanite and apatite inclusions. One hundred and thirty-one analyses yield an initial $^{177}Hf/^{176}Hf$ ratio of 3.54 ± 0.01 and an inverse isochron age of 380 ± 4 Ma (n = 131; MSWD = 1.1; Fig. 11B). Analyses with $^{176}Lu/^{177}Hf$ ratios > 50 come from the garnet core, which has Lu concentrations of 19–297 ppm. A similar inverse isochron Lu–Hf age of 373 ± 3 Ma (n = 60, MSWD = 1.3) was obtained for **apatite** in the matrix of sample Yambah (Fig. 11C). Yambah garnet has Lu contents of 0.02–297 ppm and apatite has Lu contents of 2.6–40 ppm. Six monazite grains hosted in the biotite matrix were analysed and thirty concordant analyses defined two age populations. Three analyses yielded old $^{206}Pb/^{238}U$ dates from 414 to 444 Ma, and the rest 27 analyses yielded a weighted mean average $^{206}Pb/^{238}U$ age of 370 ± 2 Ma (n = 27, MSWD = 0.65), slightly younger than the garnet and similar to the apatite Lu–Hf ages (Fig. 11D).

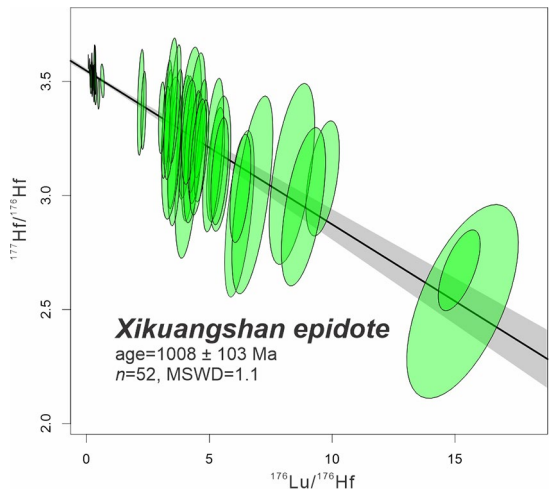

Fig. 10 Lu–Hf inverse isochron for epidote from Xikuangshan deposit

Garnet Sm–Nd geochronology was undertaken on a sample from a garnet-hornblende-staurolite-bearing schist interlayered with garnet-chlorite-allanite-bearing schist targeted for Lu-Hf dating. Ideally the same sample would be used for Sm-Nd and Lu-Hf dating, however due to the inability to remove allanite all inclusions from the garnets in the chlorite schist, an allanite-free sample of garnet-hornblende-staurolite schist from an adjacent layer in the shear zone was chosen as a comparison. Individual garnets approximately 2 mm in diameter were cut from the sample and crushed in a mortar and pestle. They were combined with magnetically separated hornblende and staurolite fractions and a whole rock. Together with the leached garnet fraction, the mineral and whole rock fractions combine to produce an age of 384.8 ± 5.2 Ma (Fig. 11E).

Coompana Province, Australia

A single **allanite** grain in **sample 4381386** from drill hole CDP004 was analysed for Lu–Hf geochronology (Fig. 7A). Thirty-one analyses were collected from this grain and they yielded Lu contents of 0.69–16 ppm and an inverse isochron Lu–Hf age of 1171 ± 35 Ma (n = 24; MSWD = 0.84; Fig. 12A). Titanite from the same sample contains varying amounts of common Pb and some evidence for potential Pb loss, i.e., deviation from the regression isochron. Analyses with potential Pb loss were excluded (dashed ellipse in Fig. 12B) and sixteen leftmost analyses on the Tera-Wasserburg plot yielded a U–Pb intercept age of 1170 ± 12 Ma (n = 16; MSWD = 0.21; Fig. 12B).

Epidote in **samples 4381382 and 4381384** from drill hole CDP001 has low $^{176}Lu/^{177}Hf$ ratios and high $^{177}Hf/^{176}Hf$ ratios, indicative of low Lu and high initial Hf concentrations typically found in epidote. Epidote from drill hole CDP001 has Lu contents of 0.03–18 ppm, predominantly lower than 4 ppm. Fifty-six analyses from session 3 yielded an inverse isochron age of 1086 ± 59 Ma (n = 56; MSWD = 1.1), and grains with higher $^{176}Lu/^{177}Hf$ ratios were analysed again in session 4. One hundred and five analyses from two sessions collectively define an inverse isochron age of 1079 ± 30 Ma (n = 105; MSWD = 1.2; Fig. 12C). Titanite from sample 4381384 yielded a U–Pb lower intercept age of 1196 ± 9 Ma (n = 31; MSWD = 1.7; Fig. 12D).

Compared to the epidote from drill hole CDP001, the **epidote** in **samples 4381389, 4381390 and 4381391** from drill hole CDP005 has lower Lu contents (0.27–19 ppm, predominantly < 2 ppm), higher initial Hf and lower $^{176}Lu/^{177}Hf$ ratios. One hundred and twelve analyses from these three samples yield an inverse isochron age of 1072 ± 60 Ma (n = 112; MSWD = 0.79; Fig. 12E). Titanite

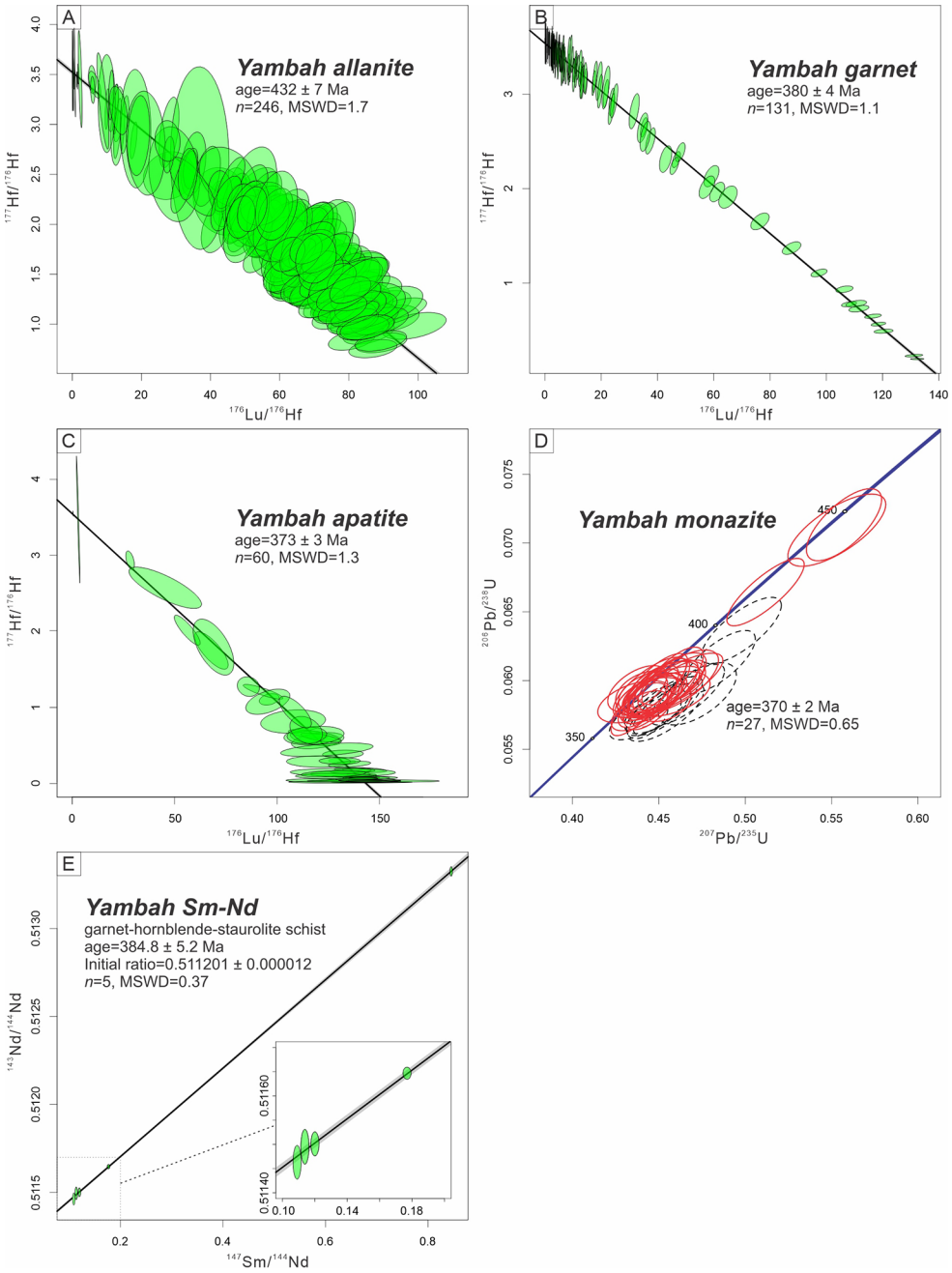

Fig. 11 Geochronology results from Yambah Shear Zone. Lu–Hf inverse isochrons for (**A**) allanite, (**B**) garnet and (**C**) apatite. (**D**) Monazite U–Pb age, discordant analyses are marked as dashed ellipses and excluded for age calculation. (**E**) Sm–Nd isochron for a garnet-hornblende-staurolite-bearing schist interlayered with garnet-chlorite-clinozoisite-bearing schist

from sample 4381389 yielded a U–Pb intercept age of 1175 ± 8 Ma ($n = 35$; MSWD = 1.3; Fig. 12F).

Discussion

Allanite, clinozoisite and epidote from various geological settings have variable Lu concentrations ranging from 0.03 to 28 ppm, thus yielding significant variability in $^{176}Lu/^{177}Hf$ ratios to define robust isochrons (Figs. 8, 9, 10, 11 and 12). In spite of the presence of common Hf in the analysed epidote group minerals and the lack of matrix matched reference materials, the Lu–Hf geochronology results corrected by Högsbo garnet have provided age constraints on magmatism, REE mineralization, metamorphism and hydrothermal alteration. In the following section, we will interpret these dates and compare Lu-Hf dates with age constraints obtained by other geochronology methods, and discuss the feasibility and geological significance of the Lu–Hf geochronology for the epidote group minerals.

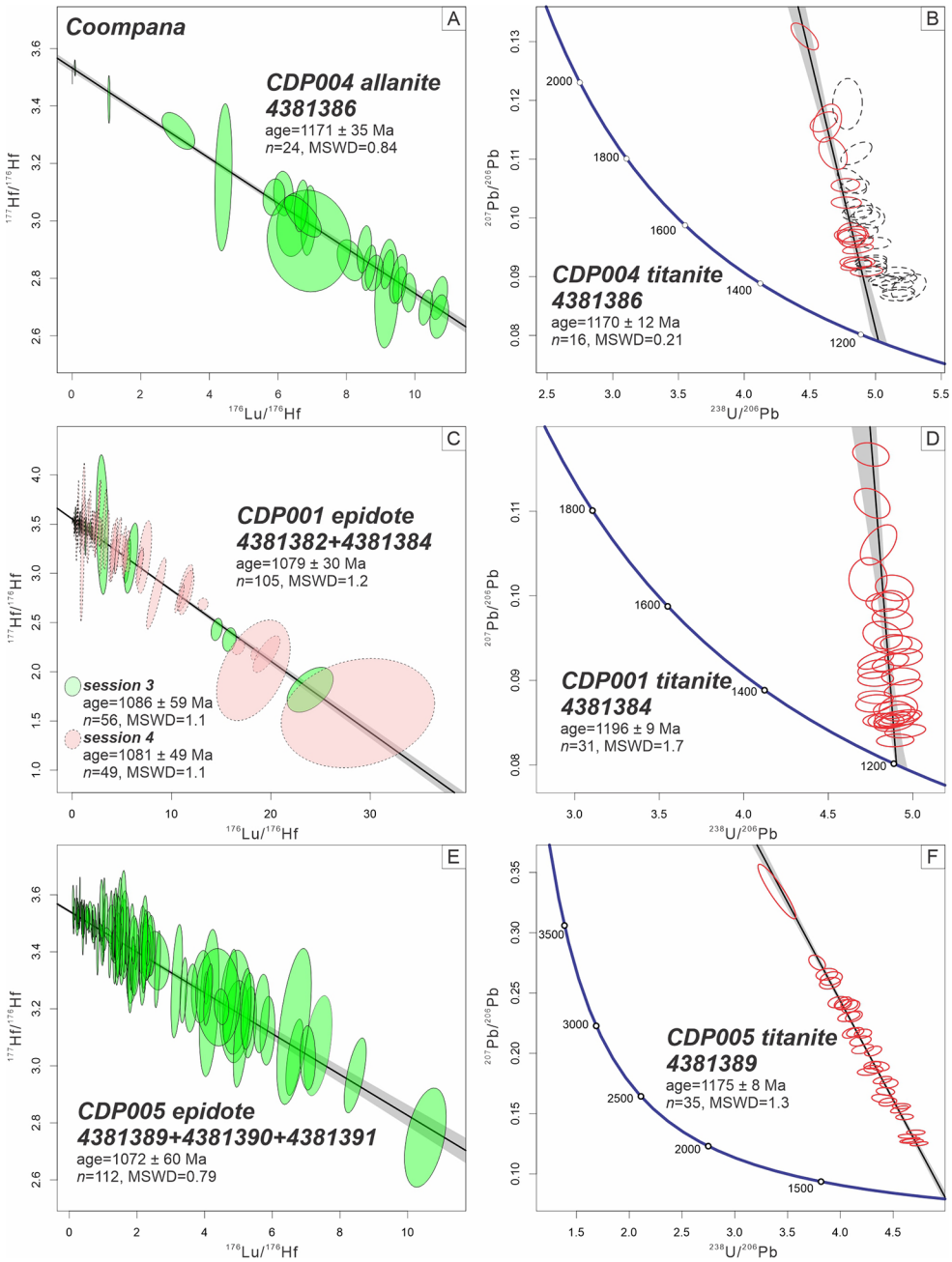

Fig. 12 Geochronology results from Coompana Province. (**A** and **B**) Allanite Lu–Hf and titanite U–Pb ages from drill hole CDP004, dashed ellipses with potential Pb loss are excluded for age calculation. (**C** and **D**) Epidote Lu–Hf and titanite U–Pb ages from drill hole CDP001, Lu–Hf data are collected from two laser sessions; (**E** and **F**) Epidote Lu–Hf and titanite U–Pb ages from drill hole CDP005

Accurate and reproducible Lu–Hf dates for magmatic and hydrothermal allanite

Mesoproterozoic magmatic allanite in the Coompana Province

Allanite can provide geochronological constraints on a range of geological processes, such as the development of magmatic systems and REE ore deposits. Four magmatic allanite samples were analysed in this study. For the Coompana Province, the allanite Lu–Hf age of 1171 ± 35 Ma, obtained for sample 4381386 in drill hole CDP004 (Lu concentrations of 0.69–16 ppm), agrees within uncertainty with the titanite U–Pb age of 1170 ± 12 Ma in the same sample (Fig. 12A and B). The newly obtained allanite and titanite ages are also consistent with the published zircon U–Pb age of 1174 ± 9 Ma for drill hole CDP004 (Jagodzinski et al. 2019), recording the crystallisation time of the monzogranite. The identical geochronology results obtained for the allanite Lu–Hf, titanite U–Pb and zircon U–Pb systems underscore the viability of in situ Lu–Hf geochronology to date allanite. The results also support the use of a garnet

reference material do date allanite, giving confidence to the calibration procedures used in this paper.

Archean magmatic allanite in the Fiskenæsset complex

The oldest allanite sample analysed in this study, LE40010 from a quartz pegmatite intruded in the Fiskenæsset anorthosite complex, yields a multi-session Lu–Hf isochron age of 2660 ± 109 Ma (Fig. 8C), which is consistent with published allanite U–Pb ages by ID-TIMS (2646 ± 94 Ma & 2735 ± 226 Ma; Smye et al. 2014) and LA-(MC)-ICP-MS (2613 ± 43 Ma & 2654 ± 63 Yang et al. 2022), and the intrusion of muscovite granite sheet at 2660 ± 20 Ma in the Fiskenæsset anorthosite complex (Pidgeon and Kalsbeek 1978). The large age uncertainty may be attributed to the low Lu concentration (1.4–1.9 ppm; Fig. 8C) and clustered Lu/Hf ratios in the allanite shard, implying that LE40010 is unsuitable for future Lu-Hf reference material.

Palaeoproterozoic magmatic and triassic hydrothermal allanite in Qingling pegmatites

Magmatic allanite samples obtained from Huayangchuan (HYC) and Huangjiagou (HJG-85, HJG-89 and HJG-90) are hosted in c. 1.81–1.83 Ga pegmatites (Yang et al. 2019; Zhang et al. 2022; Li et al. 2023), and modified by later high-temperature metamorphism and hydrothermal metasomatism (Zhang et al. 2023). For HYC allanite, anchored isochron Lu–Hf ages of 1812 ± 39 Ma and 1810 ± 32 Ma were obtained from two analytical sessions (Fig. 9A). These two ages are the same within uncertainty, demonstrating good reproducibility of the analytical method and are also consistent with published zircon U–Pb ages for the Huayangchuan pegmatites (1807 ± 14 Ma, 1826 ± 8 and 1829 ± 11 Ma; Yang et al. 2019; Li et al. 2023). Type I allanite from Huangjiagou yielded a Lu–Hf inverse isochron age of 1821 ± 74 Ma (Fig. 9C), which is also in agreement with published allanite and zircon U–Pb ages (1829 ± 23 Ma and 1826 ± 11; Zhang et al. 2022). Compared to the HYC allanite, the 1821 ± 74 Ma type I allanite from Huangjiagou has lower Lu concentrations (4.3–25 ppm for HYC vs. 0.23–4.3 ppm for Huangjiagou), inducing both lower $^{176}Lu/^{177}Hf$ ratios and lower age precision (Fig. 9A and C).

In addition, a younger generation of hydrothermal allanite (type II) was recognized at Huangjiagou and yields an inverse isochron Lu–Hf age of 215 ± 34 Ma (Fig. 9D). Despite the low accumulation of radiogenic ^{176}Hf in the young allanite, resulting in large analytical uncertainties, the allanite Lu–Hf age is notably older than the published allanite U–Pb age (131 ± 16 Ma; Zhang et al. 2023) as well as the titanite U–Pb age obtained for the same rock (131.5 ± 1.6 Ma; Fig. 9F). However, the Lu–Hf age agrees with the U–Pb age (214.1 ± 4.0 Ma) obtained for monazite inclusions within type II allanite (Figs. 3F and 9E). Type II allanite occurs along the calcite-quartz veins (Fig. 3E and F), and the c. 215 Ma ages coincide with Triassic ages widely recorded in carbonatite dykes and associated REE mineralisation in the Qinling Orogen, such as the Huayangchuan, Huanglongpu and Huangshui'an deposits (Wei et al. 2023 and references therein). Despite the presence of monazite inclusions, type II allanite contains similar REE concentrations to type I allanite (Table S2), indicating type II allanite and cogenetic monazite are not formed by recrystallisation or metasomatism of type I allanite. The relatively higher Sr and lower Zr concentrations of type II allanite (Fig. 9B) imply it may be formed by hydrothermal fluids, potentially related to the Triassic carbonatite. Hence, we interpret the Triassic type II allanite Lu-Hf age of c. 215 Ma as the timing of new generation of REE mineralisation overprinting the Huangjiagou pegmatite, while the disparate U–Pb ages obtained for titanite and allanite (Zhang et al. 2023) potentially signify later thermal disturbances during the intrusion of adjacent giant Huashan Granite batholith (Fig. 2B; zircon U-Pb ages of 142.6–132.0 Ma, zircon saturation temperatures of 727 ± 20 °C; Li et al., 2018a, b) due to their lower closure temperatures.

Prograde metamorphism recorded by allanite during Alice Springs Orogeny

Metamorphic geochronology commonly depends on the U–Th–Pb dating of accessory minerals such as zircon, monazite, xenotime and apatite. However, the (re)crystallisation of these phases during metamorphism may be hindered by unfavourable bulk-rock compositions or low metamorphic temperatures, limiting the use of these geochronometers. Allanite is a common constituent in low–medium grade metamorphosed mafic–intermediate igneous rocks, quartzofeldspathic rocks and marls. The formation of solid solutions between allanite and clinozoisite-epidote, and their ability to incorporate high contents of trace elements in their lattice make them stable over a wide range of *P*–*T* conditions (Franz and Liebscher 2004; Grapes and Hoskin 2004; Janots et al. 2008; Spear 2010). Hence, allanite geochronology (e.g., U–Th–Pb, Lu–Hf) may provide additional and unique insights into metamorphic histories (e.g., Janots et al. 2009; Gabudianu Radulescu et al. 2009; Janots and Rubatto 2014; Boston et al. 2017). Allanite from the amphibolite-facies Yambah Shear Zone, which records diachronous deformation during the Alice Springs Orogeny (Figs. 5B and 450–300 Ma; Hand and Sandiford 1999; Raimondo et al.

2014), occurrs both as inclusions in Yambah shear zone garnet and as a mineral in the shear fabric (Fig. 6), and its Lu–Hf geochronology and trace elements are used to interpret the evolution of Alice Springs Orogen.

Garnet and apatite from sample Yambah yield Lu–Hf isochron ages of c. 380–370 Ma, and the majority of monazite grains record U–Pb age of 370 Ma (Fig. 11). In comparison Sm–Nd data from garnet-hornblende-staurolite schist from an adjacent layer in the shear zone gives 383.4 ± 5.2 Ma. These c. 380 Ma ages coincide with geochronological constraints from West Bore Shear Zone and Edwards Creek Shear Zone in the Strangways Range (Fig. 5B; Möller et al. 1999; Ballèvre et al. 2000; Bendall 2000), representing the timing of peak metamorphism during the Alice Springs Orogeny (Bendall 2000). Allanite in sample Yambah, however, seems to reveal the early prograde metamorphic history of Alice Springs Orogeny. Allanite occurs within euhedral c. 380 Ma garnet and also within the chlorite-dominated foliation that wraps the garnet porphyroblasts (Fig. 6), suggesting at least part of the allanite crystallised prior to garnet growth. This interpretation is consistent with the high Lu concentrations of allanite (1.3–23 ppm, average 14 ppm) and low Lu concentration of the majority of garnet analyses (Table S2), otherwise the crystallisation of garnet would exhaust the whole rock Lu budget (Rubatto and Hermann 2007). Allanite Lu–Hf analyses produce an inverse isochron age of 432 ± 7 Ma, similar to the older monazite U–Pb dates from the Yambah Shear Zone (Fig. 11D). The associated MSWD value of 1.7, however, implies that they may not represent a statistically single age population. This could be the result of recrystallisation of some of the allanite within the foliation that wraps the garnet, meaning the analysed population of allanite has been isotopically disturbed to some extent. Conceivably the true growth age was ~ 450 Ma, consistent with the evidence elsewhere in the orogenic belt for initial shear zone formation in the late Orodvician (Fig. 5B; Mawby et al. 1999; Möller et al. 1999; Scrimgeour and Raith, 2001). Nonetheless, the bulk of the allanite is still closer in age to 450 Ma than to the age of the garnet at 380 Ma. This suggests the bulk of the matrix allanite has been inherited into the present shear fabric rather than crystallising within it. It is worth noting that apatite has higher Lu concentrations of 2.6–40 ppm with an average of 16 ppm and contradicts its younger crystallisation age than garnet. This may be attributed to Hf loss or Lu gain in apatite during c. 370 Ma tectonic or hydrothermal event, which may have also modified the monazite (Fig. 11D) but had minor effect on the allanite Lu-Hf system.

The success of allanite Lu–Hf geochronology has enabled an opportunity to obtain time constraints of major silicate phases exhibiting known *P–T* stability, thereby facilitating the integration of petrological, microstructural, and geochronological data. Considering the estimated peak *P–T* conditions of the Yambah Shear Zones at 6 kbar, 600 °C around c. 380 Ma (Bendall 2000), the retention of older allanite Lu–Hf dates suggests that its Lu–Hf system is not easily reset by amphibolite-facies prograde metamorphism. This interpretation seems consistent with the preservation of Palaeoproterozoic and Triassic ages in the Huangjiagou allanite.

Hydrothermal alteration revealed by clinozoisite and epidote

Palaeoproterozoic hydrothermal clinozoisite in the Greenland anorthosite complex

In addition to being major rock-forming minerals in magmatic and metamorphic rocks, epidote and clinozoisite are common in hydrothermal systems, occurring in veins, segregations and cavities. With the new in situ Lu–Hf dating technique, it is possible to directly date the metasomatism and fluid-rock interaction involving the formation of epidote.

Sample 207824 from the Archean anorthosite complex contains clinozoisite veins crosscutting garnet porphyroblasts and plagioclase (Fig. 2B and C). The garnet was suggested to have formed during the emplacement of the c. 3.0 Ga anorthosite complex (Windley and Smith 1974; Polat et al. 2009), however, we obtained a garnet Lu–Hf isochron age of 2577 ± 15 Ma (Fig. 8B), which corresponds to the final assembly time of the North Atlantic Craton (c. 2.56 Ga; Dyck et al. 2015), and which is within error of the emplacement of the Qôrqut Granite Complex just north of the sample location (Næraa et al. 2014). Hence garnet Lu–Hf geochronology has provided direct evidence to the metamorphism of the anorthosite complex. The clinozoisite Lu–Hf age of 2372 ± 69 Ma (Fig. 8A) is younger than the garnet age, consistent with their crosscutting relationship. This clinozoisite-bearing hydrothermal vein has been previously described in the Fiskenæsset Complex (Polat et al. 2009, 2010) but without any age constraints. For the first time, we have constrained the age of hydrothermal alteration in the Archean anorthosite complex, although its genesis and geologic significance remain unclear. Mafic dykes that intruded the Archean anorthosite complexes yielded baddeleyite U–Pb ID-TIMS ages of 2365 ± 2 Ma and 2374 ± 4 Ma (Nilsson et al. 2013). It is thus conceivable the clinozoisite alteration in anorthosite developed at the same time as the brittle faulting and mafic dyke emplacement. Considering plagioclase commonly contains limited HREE and

the small volume percent of clinozoisite (< 1%; Fig. 1B and C), Lu in the altered clinozoisite (0.27–28 ppm, average of 4.0 ppm) may have come from the hydrothermal fluids that leached HREE from the surrounding mafic rocks, or from retrograde breakdown of garnet (with Lu concentrations of 73–171 ppm) within the anorthosite.

Late mesoproterozoic hydrothermal epidote in the Coompana Province

Lu–Hf dates of 1079 ± 30 Ma and 1072 ± 60 Ma were obtained for epidote in drill holes CDP001 and CDP005 in the Coompana Province (Fig. 12C and E). These dates contrast with titanite U–Pb ages of 1196–1175 Ma (Fig. 12D and F), indicating hydrothermal alteration postdates the Moodini Supersuite magmatism. Instead, the epidote alteration may have developed during the last major magmatic episode in the Coompana Province, which is the ~ 1074 Ma intrusion of the mafic Giants Head Suite (Fig. 5C; Wise et al. 2018; Jagodzinski et al. 2019).

Late Mesoproterozoic Hydrothermal epidote in the Xikuangshan deposit

Epidote from the host rock of the Xikuangshan deposit yielded a Lu–Hf age of 1008 ± 103 Ma (Fig. 10), which is consistent with allanite U–Pb age of 1015 ± 66 Ma from the adjacent Lanniping deposit (Su et al. 2021), and c. 1.0 Ga bimodal magmatism (Zhu et al. 2016; Chen et al. 2018) and mineralisation (Chen and Zhou 2012; Li 2013) in the Kangdian IOCG province, albeit with large uncertainty due to the low Lu concentrations and $^{176}Lu/^{177}Hf$ ratios. The c. 1.0 Ga epidote at Xikuangshan may either record hydrothermal remobilisation of c. 1.7 Ga ore minerals in the system or represent a new phase of mineralisation during intracontinental rifting.

Implications for mineral exploration

As one of the most ubiquitous minerals in prophylitic alteration in porphyry ore systems and calcic alteration in IOCG systems (Groves et al. 2010; Sillitoe 2010), epidote occurrences and geochemistry have been widely used as powerful vectoring tools in mineral exploration (Cooke et al. 2014; Pacey et al. 2020; Schlegel et al. 2022). However, similar epidote-bearing assemblages can also be developed in other geologic settings, such as regional low-grade metamorphism or hydrothermal alteration caused by later intrusions. It is vital to precisely constrain the alteration time, to link epidote alteration to regional mineralisation and potential ore-causative intrusions. The epidote Lu–Hf geochronology and recently published epidote U–Pb geochronology (Peverelli et al. 2021) complement each other, considering two isotopic systems may have different parent-to-daughter ratios and different closure temperatures, and thus assist differentiation of prophylitic/calcic alteration in ore systems from similar assemblages developed during non-mineralising processes. In addition, the novel in situ method does not require mineral separation or dissolution, providing the ability to quickly obtain large Lu–Hf geochronology datasets during mineral exploration. In addition to calcite and fluorite Lu–Hf geochronology (Simpson et al. 2022; Glorie et al. 2023a), epidote Lu–Hf dating opens up new opportunities to a wide range of applications for future exploration programs.

Current limitations

In contrast to (felsic) apatite, calcite and fluorite which do not incorporate significant concentrations of common Hf (Simpson et al. 2022; Glorie et al. 2023b), epidote group minerals, including allanite, can incorporate varying amounts of common Hf (Figs. 8, 9, 10, 11 and 12). As a result, the success rate of the Lu–Hf dating approach in epidote group minerals is intrinsically related to both the concentration of Lu and the ingrowth time for radiogenic Hf (Simpson et al. 2021, 2022). Magmatic and metamorphic allanite in low- to medium-grade metamorphic rocks may act as primary REE reservoirs, which often have Lu concentrations high enough for Lu–Hf geochronology. However, caution may be required in the selection of hydrothermal epidote samples, especially when epidote has a high modal proportion in a given rock. Large volumes of epidote would dilute Lu concentrations in a laser target, unless the hydrothermal fluids that conditioned crystallisation of epidote are Lu-rich. Hence, pre-screening of Lu-rich samples is recommended to identify grains or zones with high $^{176}Lu/^{177}Hf$ ratios (Table S2). Targeting such Lu-rich zones can significantly reduce the final age uncertainties (Fig. 12C). The use of large laser beam spot sizes can also significantly improve precision at the expense of lower spatial resolution. In this study, age precisions of 4–10% can be achieved for epidote samples with Lu concentrations as low as 1–2 ppm (Figs. 10 and 12E).

Another current limitation for Lu–Hf geochronology applied to epidote group minerals is the lack of suitable (matrix-matched) reference materials. In this paper, garnet reference materials Högsbo and Black Point were employed to correct and monitor the matrix-induced fractionation. While garnet is not an epidote-group mineral, it appears to have similar ablation characteristics. The agreement observed between allanite and epidote Lu–Hf ages and those obtained through other geochronological methods underscores the suitability of garnet as a reference material

for epidote-group Lu–Hf dating. However, detailed characterisation of garnet crystals is required as they may have highly variable Lu concentrations such as the Högsbo garnet (Simpson et al. 2021). Appropriate spots sizes are required to measure the garnet reference materials and samples in the same detector mode (Glorie et al. 2024), i.e., pulse mode based on the ^{175}Lu count rates (< 1 Mcps) of all analysed epidote group minerals in this study. There is potential for improvement when suitable reference materials can be identified. For instance, Lu-rich allanite from pegmatites, particularly when not subjected to complex post-crystallisation alteration, holds promise as a closely matrix-matched reference material for epidote group minerals.

Conclusion

This study presents the first Lu–Hf dating of epidote group minerals by LA-ICP-MS/MS. Allanite, epidote and clinozoisite from a variety of geological environments yielded meaningful ages consistent with those from other geochronological methods, demonstrating the feasibility of the epidote group minerals Lu–Hf method. Magmatic allanite samples from pegmatite and monzogranite yielded Lu–Hf dates in agreement with the timing of magmatism in the Fiskenæsset complex, Coompana Province and Qingling Orogen. Additionally, Lu–Hf dates for hydrothermal allanite agree with the timing of REE mineralisation in the Qinling Orogen. Metamorphic allanite from the Yambah Shear Zone yielded Lu–Hf ages that are c. 50 Ma older than the c. 380 Ma peak metamorphism of the Alice Springs Orogeny, suggesting preservation of older dates during prograde metamorphism. Allanite Lu–Hf system remains closed during amphibolite-facies metamorphism at conditions of 6 kbar, 600 °C. Hydrothermal clinozoisite and epidote provided time constraints for fluid-rock interactions and hydrothermal mineralisation in a range of settings, demonstrating the utility of the technique for mineral exploration.

Supplementary Information The online version contains supplementary material available at https://doi.org/10.1007/s00410-024-02143-y.

Acknowledgements The authors would like to thank the Mineral Exploration Cooperative Research Centre (MinEx CRC) and the Australian Research Council (ARC DP200101881) for funding this research. B. Wade and B. Cave are thanked for their technical support at Adelaide Microscopy. Dr X.F. He is thanked for collecting the monazite data from Yambah. Dr H. Zheng, Mr H.X. Zhang, and Mr X.Q. Yin are thanked for the sharing of allanite/epidote samples. Professor Daniela Rubatto is thanked for thorough and efficient handling of the manuscript during review. Professor Stéphanie Duchene and Dr Lorraine Tual are thanked for constructive feedback during review.

Funding Open Access funding enabled and organized by CAUL and its Member Institutions.
Open Access funding enabled and organized by CAUL and its Member Institutions

References

Baadsgaard H, McGregor VR (1981) The U-th-pb systematics of zircons from the type Nûk gneisses, Godthåbsfjord, West Greenland. Geochim Cosmochim Acta 45(7):1099–1109. https://doi.org/10.1016/0016-7037(81)90134-4

Ballèvre M, Möller A, Hensen BJ (2000) Exhumation of the lower crust during crustal shortening: an Alice Springs (380 Ma) age for a prograde amphibolite facies shear zone in the Strangways Metamorphic Complex (central Australia). J Metamorph Geol 18(6):737–747. https://doi.org/10.1046/j.1525-1314.2000.00289.x

Barth S, Oberli F, Meier M (1994) ThPb versus UPb isotope systematics in allanite from co-genetic rhyolite and granodiorite: implications for geochronology. Earth Planet Sci Lett 124(1):149–159. https://doi.org/10.1016/0012-821X(94)00073-5

Bedoya A, Glorie S, Hand M, Kirkland CL, Kelsey DE, Nixon A, Fraser G (2024) Apatite Triple dating (Lu–Hf, U–Pb, FT) constrains deformation and cooling in the Coompana and Madura Provinces, Western Australia. Lithosphere 2023(Special 14lithosphere20232292. https://doi.org/10.2113/2023/lithosphere_2023_292

Bendall B (2000) Mid-Palaeozoic shear zones in the Strangways Range: a record of intracratonic tectonism in the Arunta Inlier, central Australia. PhD Thesis. University of Adelaide

Bird DK, Spieler AR (2004) Epidote in Geothermal systems. Rev Mineral Geochem 56(1):235–300. https://doi.org/10.2138/gsrmg.56.1.235

Boston KR, Rubatto D, Hermann J, Engi M, Amelin Y (2017) Geochronology of accessory allanite and monazite in the Barrovian metamorphic sequence of the Central Alps, Switzerland. Lithos 286–287:502–518. https://doi.org/10.1016/j.lithos.2017.06.025

Brown DA, Simpson A, Hand M, Morrissey LJ, Gilbert S, Tamblyn R, Glorie S (2022) Laser-ablation Lu-Hf dating reveals Laurentian Garnet in subducted rocks from southern Australia. Geology 50(7):837–842

Buick IS, Frei R, Cartwright I (1999) The timing of high-temperature retrogression in the Reynolds Range, central Australia: constraints from garnet and epidote Pb-Pb dating. Contrib Miner Petrol 135(2):244–254. https://doi.org/10.1007/s004100050510

Catlos EJ, Sorensen SS, Harrison TM (2000) Th-Pb ion-microprobe dating of allanite. Am Mineral 85(5–6):633–648. https://doi.org/10.2138/am-2000-5-601

Chen YJ, Santosh M (2014) Triassic tectonics and mineral systems in the Qinling Orogen, central China. Geol J 49(4–5):338–358. https://doi.org/10.1002/gj.2618

Chen WT, Zhou MF (2012) Paragenesis, stable isotopes, and Molybdenite Re-os Isotope Age of the Lala Iron-Copper Deposit, Southwest China. Econ Geol 107(3):459–480. https://doi.org/10.2113/econgeo.107.3.459

Chen WT, Zhou MF (2014) Ages and compositions of primary and secondary allanite from the Lala Fe–Cu deposit, SW China: implications for multiple episodes of hydrothermal events. Contrib Miner Petrol 168(2):1043. https://doi.org/10.1007/s00410-014-1043-1

Chen WT, Sun WH, Wang W, Zhao JH, Zhou MF (2014) Grenvillian intra-plate mafic magmatism in the southwestern Yangtze Block, SW China. Precambrian Res 242:138–153

Chen WT, Sun WH, Zhou MF, Wang W (2018) Ca. 1050 Ma intra-continental rift-related A-type felsic rocks in the southwestern Yangtze Block, South China. Precambrian Res 309:22–44. https://doi.org/10.1016/j.precamres.2017.02.011

Claoué-Long J, Maidment D, Hussey K, Huston D (2008) The duration of the strangways Event in central Australia: evidence for prolonged deep crust processes. Precambrian Res 166(1):246–262. https://doi.org/10.1016/j.precamres.2007.06.023

Cooke DR, Baker M, Hollings P, Sweet G, Chang Z, Danyushevsky L, Gilbert S, Zhou T, White NC, Gemmell JB, Inglis S (2014) New advances in detecting the distal geochemical footprints of Porphyry systems—Epidote Mineral Chemistry as a Tool for Vectoring and Fertility assessments. In: Kelley KD, Golden HC (eds) Building Exploration Capability for the 21st Century, vol 18. Society of Economic Geologists

Deer W, Howie R, Zussman J (1986) Disilicates and Ring silicates (Rock-Forming minerals: volume 1B). In. vol. Geological Society of London

Dutch RA (2018) Coompana Province geochemistry and petrogenesis. In: Dutch RA, Wise TW, Pawley MJ, and Petts A (eds) Coompana Drilling and Geochemistry Workshop 2018 extended abstracts, Volume Report Book 2018/00019, Department for Energy and Mining, South Australia, Report Book 2018/00019, Adelaide, pp 76–101

Dyck B, Reno BL, Kokfelt TF (2015) The Majorqaq Belt: a record of Neoarchaean orogenesis during final assembly of the North Atlantic Craton, southern West Greenland. Lithos 220–223:253–271. https://doi.org/10.1016/j.lithos.2015.01.024

Dziggel A, Diener JFA, Kolb J, Kokfelt TF (2014) Metamorphic record of accretionary processes during the Neoarchaean: the Nuuk region, southern West Greenland. Precambrian Res 242:22–38. https://doi.org/10.1016/j.precamres.2013.12.010

El Korh A (2014) Ablation behaviour of allanites during U–Th–Pb dating using a quadrupole ICP-MS coupled to a 193nm excimer laser. Chem Geol 371:46–59. https://doi.org/10.1016/j.chemgeo.2014.01.021

Enami M, Liou JG, Mattinson CG (2004) Epidote Minerals in High P/T Metamorphic terranes: Subduction Zone and High- to Ultra-high-pressure metamorphism. Rev Mineral Geochem 56(1):347–398. https://doi.org/10.2138/gsrmg.56.1.347

Fournier HW, Camacho A, Lee JKW (2016) High-strain deformation and fluid infiltration diachronism of the middle crust: New Devonian–Permian Alice Springs ages (365–290 ma) of shear zones in the Strangways Metamorphic Complex, Central Australia. Chem Geol 443:39–53. https://doi.org/10.1016/j.chemgeo.2016.09.014

Franz G, Liebscher A (2004) Physical and chemical properties of the epidote minerals–An Introduction–. Rev Mineral Geochem 56(1):1–81

Frei D, Liebscher A, Franz G, Dulski P (2004) Trace Element Geochemistry of Epidote Minerals. Rev Mineral Geochem 56(1):553–605. https://doi.org/10.2138/gsrmg.56.1.553

Gabudianu Radulescu I, Rubatto D, Gregory C, Compagnoni R (2009) The age of HP metamorphism in the Gran Paradiso Massif, Western Alps: a petrological and geochronological study of silvery micaschists. Lithos 110(1):95–108. https://doi.org/10.1016/j.lithos.2008.12.008

Gieré R, Sorensen SS (2004) Allanite and other REE-Rich Epidote-Group minerals. Rev Mineral Geochem 56(1):431–493. https://doi.org/10.2138/gsrmg.56.1.431

Glorie S, Burke T, Hand M, Simpson A, Gilbert S, Wade B (2022a) In situ Lu–Hf phosphate geochronology: Progress towards a new tool for space exploration. Geosci Front 13(3):101375. https://doi.org/10.1016/j.gsf.2022.101375

Glorie S, Gillespie J, Simpson A, Gilbert S, Khudoley A, Priyatkina N, Hand M, Kirkland Christopher L (2022b) Detrital apatite Lu–Hf and U–Pb geochronology applied to the southwestern siberian margin. Terra Nova 34(3):201–209. https://doi.org/10.1111/ter.12580

Glorie S, Hand M, Mulder J, Simpson A, Emo Robert B, Kamber B, Fernie N, Nixon A, Gilbert S (2023a) Robust laser ablation Lu–Hf dating of apatite: an empirical evaluation. Geological Society, London, Special Publications 537(1):SP537-2022-2205 https://doi.org/10.1144/SP537-2022-205

Glorie S, Mulder J, Hand M, Fabris A, Simpson A, Gilbert S (2023b) Laser ablation (in situ) Lu-Hf dating of magmatic fluorite and hydrothermal fluorite-bearing veins. Geosci Front 14(6):101629. https://doi.org/10.1016/j.gsf.2023.101629

Glorie S, Simpson A, Gilbert SE, Hand M, Müller AB (2024) Testing the reproducibility of in situ LuHf dating using Lu-rich garnet from the Tørdal pegmatites, southern Norway. Chem Geol 653:122038. https://doi.org/10.1016/j.chemgeo.2024.122038

Grapes RH, Hoskin PWO (2004) Epidote Group Minerals in low–medium pressure metamorphic terranes. Rev Mineral Geochem 56(1):301–345. https://doi.org/10.2138/gsrmg.56.1.301

Greentree MR, Li Z-X, Li X-H, Wu H (2006) Late mesoproterozoic to earliest neoproterozoic basin record of the Sibao orogenesis in western South China and relationship to the assembly of Rodinia. Precambrian Res 151(1):79–100. https://doi.org/10.1016/j.precamres.2006.08.002

Gregory CJ, Rubatto D, Allen CM, Williams IS, Hermann J, Ireland T (2007) Allanite micro-geochronology: a LA-ICP-MS and SHRIMP U–Th–Pb study. Chem Geol 245(3):162–182. https://doi.org/10.1016/j.chemgeo.2007.07.029

Gregory CJ, Rubatto D, Hermann J, Berger A, Engi M (2012) Allanite behaviour during incipient melting in the southern Central Alps. Geochim Cosmochim Acta 84:433–458. https://doi.org/10.1016/j.gca.2012.01.020

Groves DI, Bierlein FP, Meinert LD, Hitzman MW (2010) Iron Oxide Copper-Gold (IOCG) deposits through Earth History: implications for Origin, Lithospheric setting, and distinction from other Epigenetic Iron Oxide deposits. Econ Geol 105(3):641–654. https://doi.org/10.2113/gsecongeo.105.3.641

Hand M, Sandiford M (1999) Intraplate deformation in central Australia, the link between subsidence and fault reactivation. Tectonophysics 305(1):121–140. https://doi.org/10.1016/S0040-1951(99)00009-8

Hartnady MIH, Kirkland CL, Dutch RA, Bodorkos S, Jagodzinski EA (2020) Evaluating zircon initial hf isotopic composition using a combined SIMS–MC-LASS-ICP-MS approach: a case study from the Coompana Province in South Australia. Chem Geol 558:119870. https://doi.org/10.1016/j.chemgeo.2020.119870

Hoffmann JE, Svahnberg H, Piazolo S, Scherstén A, Münker C (2012) The geodynamic evolution of Mesoarchean anorthosite complexes inferred from the Naajat Kuuat Complex, southern West

Greenland. Precambrian Res 196–197:149–170. https://doi.org/10.1016/j.precamres.2011.12.002
Jagodzinski EA, Pawley M, Wise T, Bodorkos S, Crowley JL (2019) PACE copper Coompana Drilling Project: U-Pb dating of basement and cover rocks. Department for Energy and Mining, South Australia. Report Book 2018/00028
Janots E, Rubatto D (2014) U–Th–Pb dating of collision in the external Alpine domains (Urseren Zone, Switzerland) using low temperature allanite and monazite. Lithos 184–187:155–166. https://doi.org/10.1016/j.lithos.2013.10.036
Janots E, Engi M, Berger A, Allaz J, Schwarz JO, Spandler C (2008) Prograde metamorphic sequence of REE minerals in pelitic rocks of the Central Alps: implications for allanite–monazite–xenotime phase relations from 250 to 610°C. J Metamorph Geol 26(5):509–526. https://doi.org/10.1111/j.1525-1314.2008.00774.x
Janots E, Engi M, Rubatto D, Berger A, Gregory C, Rahn M (2009) Metamorphic rates in collisional orogeny from in situ allanite and monazite dating. Geology 37(1):11–14. https://doi.org/10.1130/G25192A.1
Kirkland CL, Smithies RH, Spaggiari CV, Wingate MTD, Quentin de Gromard R, Clark C, Gardiner NJ, Belousova EA (2017) Proterozoic crustal evolution of the Eucla basement, Australia: implications for destruction of oceanic crust during emergence of Nuna. Lithos 278–281:427–444. https://doi.org/10.1016/j.lithos.2017.01.029
Li YL (2013) The study of geological-geochemical features and the model of ore-controlling structure in the Xikuangshan type copper-ferro deposit, Dongchuan, Yunnan Province. PhD Thesis. Kunming University of Science and Technology
Li Y, Vermeesch P (2021) Short communication: inverse isochron regression for Re–Os, K–Ca and other chronometers. Geochronology 3(2):415–420. https://doi.org/10.5194/gchron-3-415-2021
Li XC, Zhou MF (2018b) The Nature and Origin of Hydrothermal REE Mineralisation in the sin Quyen Deposit, Northwestern Vietnam. Econ Geol 113(3):645–673. https://doi.org/10.5382/econgeo.2018.4565
Li Z, Wang J, Liu J, Li C, Du A, Liu Y, Ye L (2003) Re-os dating of molybdenite from Lala Fe-oxide-Cu-Au-Mo-REE deposit, southwest China: implications for ore genesis. Contrib Geol Mineral Resour Res 18(1):39–42 (in Chinese with English abstract)
Li N, Chen Y-J, Santosh M, Pirajno F (2018a) Late mesozoic granitoids in the Qinling Orogen, Central China, and tectonic significance. Earth Sci Rev 182:141–173. https://doi.org/10.1016/j.earscirev.2018.05.004
Li P, Li Y, Gu P, He S, Zhuang Y, Chen R (2023) Paleoproterozoic U mineralisation in Huayangchuan Deposit, Xiaoqinling Area: evidence from the U-Rich Granitic Pegmatite. Minerals 13:936. https://doi.org/10.3390/min13070936
Maidment DW (2005) Palaeozoic high-grade metamorphism within the Centralian Superbasin, Harts Range region, central Australia. Australian National University
Mawby J, Hand M, Foden J (1999) Sm–Nd evidence for high-grade Ordovician metamorphism in the Arunta Block, central Australia. J Metamorph Geol 17(6):653–668. https://doi.org/10.1046/j.1525-1314.1999.00224.x
Möller A, Armstrong R, Hensen B, Williams I (1999) Dating metamorphic events & deformation; SHRIMP U-Pb zircon examples from the Strangways metamorphic complex, Arunta Inlier, Australia. In: European Union of Geosciences conference, Abstr, vol 4
Myers JS (1985) Stratigraphy and structure of the Fiskenæsset Complex, southern West Greenland. Bull Grønlands Geologiske Undersøgelse 150:1–72. https://doi.org/10.34194/bullggu.v150.6692
Næraa T, Kemp AIS, Scherstén A, Rehnström EF, Rosing MT, Whitehouse MJ (2014) A lower crustal mafic source for the ca. 2550 Ma Qôrqut Granite Complex in southern West Greenland. Lithos 192–195:291–304. https://doi.org/10.1016/j.lithos.2014.02.013
Nebel O, Morel ML, Vroon PZ (2009) Isotope dilution determinations of Lu, Hf, Zr, Ta and W, and Hf isotope compositions of NIST SRM 610 and 612 glass wafers. Geostand Geoanal Res 33(4):487–499
Nilsson MKM, Klausen MB, Söderlund U, Ernst RE (2013) Precise U–Pb ages and geochemistry of Palaeoproterozoic mafic dykes from southern West Greenland: linking the North Atlantic and the Dharwar cratons. Lithos 174:255–270. https://doi.org/10.1016/j.lithos.2012.07.021
Norris A, Danyushevsky L (2018) Towards estimating the complete uncertainty budget of quantified results measured by LA-ICP-MS. Goldschmidt: Boston, MA, USA
Oberli F, Meier M, Berger A, Rosenberg CL, GierÉ R (2004) U-th-pb and 230Th/238U disequilibrium isotope systematics: precise accessory mineral chronology and melt evolution tracing in the Alpine Bergell intrusion. Geochim Cosmochim Acta 68(11):2543–2560. https://doi.org/10.1016/j.gca.2003.10.017
Pacey A, Wilkinson JJ, Cooke DR (2020) Chlorite and Epidote Mineral Chemistry in Porphyry Ore systems: a case study of the Northparkes District, New South Wales, Australia. Econ Geol 115(4):701–727. https://doi.org/10.5382/econgeo.4700
Pawley M, Dutch R, Wise T, Reid A (2018) The Coompana Province: structural insights and prospectivity. Geological survey of South Australia Discovery Day 2018: presentation abstracts and posters. vol. Department for Energy and Mining South Australia, pp 19–24
Pawley MJ, Dutch RA, Wise TW (2020a) The relationship between Crustal Architecture, deformation, and Magmatism in the Coompana Province, Australia. Tectonics 39(12). https://doi.org/10.1029/2019TC005593. e2019TC005593 doi
Pawley MJ, Wise TW, Dutch RA, Jagodzinski EA (2020b) New Proterozoic stratigraphic units of the Coompana Province of South Australia. MESA J 93(2):4–23
Payne JL, Hand M, Barovich KM, Wade BP (2008) Temporal constraints on the timing of high-grade metamorphism in the northern Gawler Craton: implications for assembly of the Australian Proterozoic. Aust J Earth Sci 55(5):623–640. https://doi.org/10.1080/08120090801982595
Peverelli V, Ewing T, Rubatto D, Wille M, Berger A, Villa IM, Lanari P, Pettke T, Herwegh M (2021) U – pb geochronology of epidote by laser ablation inductively coupled plasma mass spectrometry (LA-ICP-MS) as a tool for dating hydrothermal-vein formation. Geochronology 3(1):123–147. https://doi.org/10.5194/gchron-3-123-2021
Pidgeon RT, Kalsbeek F (1978) Dating of igneous and metamorphic events in the Fiskenaesset region of southern west Greenland. Can J Earth Sci 15(12):2021–2025. https://doi.org/10.1139/e78-211
Polat A, Appel PWU, Fryer B, Windley B, Frei R, Samson IM, Huang H (2009) Trace element systematics of the Neoarchean Fiskenæsset anorthosite complex and associated meta-volcanic rocks, SW Greenland: evidence for a magmatic arc origin. Precambrian Res 175(1):87–115. https://doi.org/10.1016/j.precamres.2009.09.002
Polat A, Frei R, Scherstén A, Appel PWU (2010) New age (ca. 2970 Ma), mantle source composition and geodynamic constraints on the Archean Fiskenæsset anorthosite complex, SW Greenland. Chem Geol 277(1):1–20. https://doi.org/10.1016/j.chemgeo.2010.06.016
Raimondo T, Hand M, Collins WJ (2014) Compressional intracontinental orogens: ancient and modern perspectives. Earth Sci Rev 130:128–153. https://doi.org/10.1016/j.earscirev.2013.11.009
Romer RL, Smeds S-A (1996) U-Pb columbite ages of pegmatites from Sveconorwegian terranes in southwestern Sweden. Precambrian Res 76(1):15–30. https://doi.org/10.1016/0301-9268(95)00023-2

Rubatto D, Hermann J (2007) Experimental zircon/melt and zircon/garnet trace element partitioning and implications for the geochronology of crustal rocks. Chem Geol 241(1):38–61. https://doi.org/10.1016/j.chemgeo.2007.01.027

Schlegel TU, Birchall R, Shelton TD, Austin JR, Mapping the mineral zonation at the ernest henry iron oxide copper-gold deposit (2022) vectoring to Cu-Au mineralisation using modal mineralogy. Econ Geol 117(2):485–494. https://doi.org/10.5382/econgeo.4915

Schmidt MW, Poli S (2004) Magmatic epidote. Rev Mineral Geochem 56(1):399–430. https://doi.org/10.2138/gsrmg.56.1.399

Scrimgeour I, Raith Johann G (2001) High-grade reworking of Proterozoic granulites during Ordovician intraplate transpression, eastern Arunta Inlier, central Australia. Geological Society, London, Special Publications 184(1):261–287 https://doi.org/10.1144/GSL.SP.2001.184.01.13

Sillitoe RH (2010) Porphyry Copper systems. Econ Geol 105(1):3–41. https://doi.org/10.2113/gsecongeo.105.1.3

Simpson A, Gilbert S, Tamblyn R, Hand M, Spandler C, Gillespie J, Nixon A, Glorie S (2021) In-situ Lu Hf geochronology of garnet, apatite and xenotime by LA ICP MS/MS. Chem Geol 577. https://doi.org/10.1016/j.chemgeo.2021.120299

Simpson A, Glorie S, Hand M, Spandler C, Gilbert S, Cave B (2022) In situ Lu–Hf geochronology of calcite. Geochronology 4(1):353–372. https://doi.org/10.5194/gchron-4-353-2022

Smye AJ, Roberts NMW, Condon DJ, Horstwood MSA, Parrish RR (2014) Characterising the U–Th–Pb systematics of allanite by ID and LA-ICPMS: implications for geochronology. Geochim Cosmochim Acta 135:1–28. https://doi.org/10.1016/j.gca.2014.03.021

Söderlund U, Patchett PJ, Vervoort JD, Isachsen CE (2004) The 176Lu decay constant determined by Lu–Hf and U–Pb isotope systematics of precambrian mafic intrusions. Earth Planet Sci Lett 219(3–4):311–324

Spaggiari CV, Smithies RH, Kirkland CL, Wingate MTD, England RN, Lu Y (2020) Stratigraphic and co-funded drilling of the Eucla basement — the Proterozoic geology beneath the Nullarbor Plain, Geological Survey of Western Australia, Report 204, Perth

Spandler C, Hammerli J, Sha P, Hilbert-Wolf H, Hu Y, Roberts E, Schmitz M (2016) MKED1: a new titanite standard for in situ analysis of Sm–Nd isotopes and U–Pb geochronology. Chem Geol 425:110–126. https://doi.org/10.1016/j.chemgeo.2016.01.002

Spear FS (2010) Monazite–allanite phase relations in metapelites. Chem Geol 279(1):55–62. https://doi.org/10.1016/j.chemgeo.2010.10.004

Spencer CJ, Kirkland CL, Roberts NMW, Evans NJ, Liebmann J (2020) Strategies towards robust interpretations of in situ zircon Lu–Hf isotope analyses. Geosci Front 11(3):843–853. https://doi.org/10.1016/j.gsf.2019.09.004

Su ZK, Zhao XF, Li XC, Zhou MF, Kennedy AK, Zi JW, Spandler C, Yang YH, Unraveling mineralisation and multistage hydrothermal overprinting histories by integrated in situ U-Pb and, Sm-Nd (2021) isotopes in a paleoproterozoic breccia-hosted iocg deposit, Sw China. Econ Geol 116(7):1687–1710 doi:https://doi.org/10.5382/econgeo.4840

Symington NJ, Weinberg RF, Hasalová P, Wolfram LC, Raveggi M, Armstrong RA (2014) Multiple intrusions and remelting-remobilization events in a magmatic arc: the St. Peter suite, South Australia. GSA Bull 126(9–10):1200–1218. https://doi.org/10.1130/B30975.1

Tamblyn R, Hand M, Simpson A, Gilbert S, Wade B, Glorie S (2022) In situ laser ablation Lu–Hf geochronology of garnet across the western Gneiss Region: campaign-style dating of metamorphism. J Geol Soc 179(4):jgs2021–2094. https://doi.org/10.1144/jgs2021-094

Thompson J, Meffre S, Maas R, Kamenetsky V, Kamenetsky M, Goemann K, Ehrig K, Danyushevsky L (2016) Matrix effects in Pb/U measurements during LA-ICP-MS analysis of the mineral apatite. J Anal at Spectrom 31(6):1206–1215

Vermeesch P (2018) IsoplotR: a free and open toolbox for geochronology. Geosci Front 9(5):1479–1493

Vermeesch P (2024) (anchored) isochrons in IsoplotR. Geochronol Discuss 2024:1–16. https://doi.org/10.5194/gchron-2024-5

Villa IM, Holden NE, Possolo A, Ickert RB, Hibbert DB, Renne PR (2020) IUPAC-IUGS recommendation on the half-lives of 147Sm and 146Sm. Geochim Cosmochim Acta 285:70–77. https://doi.org/10.1016/j.gca.2020.06.022

Wei CW, Xu C, Song WL, Chen W, Shi A, Li Z, Fan C (2023) Heavy rare earth element and crustal-derived silicon enrichment in Huayangchuan carbonatites, Qinling orogenic belt. Lithos. https://doi.org/10.1016/j.lithos.2022.106987. 436–437:106987 doi

Whitney DL, Evans BW (2010) Abbreviations for names of rock-forming minerals. Am Mineral 95(1):185–187. https://doi.org/10.2138/am.2010.3371

Windley BF, Garde AA (2009) Arc-generated blocks with crustal sections in the North Atlantic craton of West Greenland: crustal growth in the Archean with modern analogues. Earth Sci Rev 93(1):1–30. https://doi.org/10.1016/j.earscirev.2008.12.001

Windley BF, Smith JV (1974) The Fiskenæsset complex, West Greenland. Part II. General mineral chemistry from Qeqertarssuatsiaq. Bull Grønlands Geologiske Undersøgelse 108:1–50

Wise T, Dutch R, Pawley M, Foss C, Thiel S (2018) Building the Coompana Province. MESA J 88(3):25–37

Yang C, Zhao L, Zheng H, Wang D (2019) The multiple granitic magmatism in the giant Huayangchuan uranium polymetallic ore district: implications for tectonic evolution of the southern margin of North China Craton in the Qinling Orogen. Ore Geol Rev 112:103055. https://doi.org/10.1016/j.oregeorev.2019.103055

Yang M, Yang YH, Kamo SL, Romer RL, Roberts NMW, Wang H, Xie LW, Huang C, Yang JH, Wu FY (2022) Natural Allanite reference materials for In Situ U-Th-Pb and Sm-Nd isotopic measurements by LA-(MC)-ICP-MS. Geostand Geoanal Res 46(2):169–203. https://doi.org/10.1111/ggr.12417

Zhang HX, Jiang SY, Yuan F, Liu SQ (2022) LA-(MC)-ICP-MS u-th-pb dating and nd isotopes of allanite in NYF pegmatite from lesser qingling orogenic belt, central China. Ore Geol Rev 145. https://doi.org/10.1016/j.oregeorev.2022.104893

Zhang HX, Jiang SY, Liu SQ, Yuan F (2023) Sm-Nd and U-Pb isotope behavior of REE-rich accessory minerals in pegmatite during overprinted metamorphic and hydrothermal events: evidence from the Paleoproterozoic rare-earth pegmatite in the lesser Qinling district of China. Precambrian Res 389. https://doi.org/10.1016/j.precamres.2023.107020

Zhao XF, Zhou MF (2011) Fe–Cu deposits in the Kangdian region, SW China: a proterozoic IOCG (iron-oxide–copper–gold) metallogenic province. Miner Deposita 46(7):731–747. https://doi.org/10.1007/s00126-011-0342-y

Zhao XF, Zhou MF, Li JW, Sun M, Gao JF, Sun WH, Yang JH (2010) Late Paleoproterozoic to early Mesoproterozoic Dongchuan Group in Yunnan, SW China: implications for tectonic evolution of the Yangtze Block. Precambrian Res 182(1):57–69. https://doi.org/10.1016/j.precamres.2010.06.021

Zhao XF, Zhou MF, Li JW, Selby D, Li XH, Qi L (2013) Sulfide Re-Os and, Rb-Sr Isotope dating of the kangdian iocg metallogenic province, Southwest China: Implications for regional metallogenesis. Econ Geol 108(6):1489–1498. https://doi.org/10.2113/econgeo.108.6.1489

Zhao H, Jiang S, Dai B, Ma L, Li J (2015) Geochronology and Hf isotope study of pegmatite in the Xiaoqinling area of NW China: implication for petrogenesis and regional metamorphism. J Earth Sci 26(3):295–305. https://doi.org/10.1007/s12583-015-0537-8

Zhao XF, Zhou MF, Su ZK, Li XC, Chen WT, Li JW (2017) Geology, Geochronology, and Geochemistry of the Dahongshan

Fe-Cu-(Au-Ag) Deposit, Southwest China: implications for the formation of Iron Oxide Copper-Gold deposits in Intracratonic Rift settings. Econ Geol 112(3):603–628. https://doi.org/10.2113/econgeo.112.3.603

Zheng H, Chen H, Wu C, Jiang H, Gao C, Kang Q, Yang C, Wang D, Lai C-k (2020) Genesis of the supergiant Huayangchuan carbonatite-hosted uranium-polymetallic deposit in the Qinling Orogen, Central China. Gondwana Res 86:250–265. https://doi.org/10.1016/j.gr.2020.05.016

Zhou MF, Zhao XF, Chen WT, Li XC, Wang W, Yan DP, Qiu HN (2014) Proterozoic Fe–Cu metallogeny and supercontinental cycles of the southwestern Yangtze Block, southern China and northern Vietnam. Earth Sci Rev 139:59–82. https://doi.org/10.1016/j.earscirev.2014.08.013

Zhu WG, Zhong H, Li ZX, Bai ZJ, Yang YJ (2016) SIMS zircon U–Pb ages, geochemistry and Nd–Hf isotopes of ca. 1.0Ga mafic dykes and volcanic rocks in the Huili area, SW China: origin and tectonic significance. Precambrian Res 273:67–89. https://doi.org/10.1016/j.precamres.2015.12.011